

Award Number: W81XWH-13-1-0127

TITLE: Magnetic Resonance-Based Electrical Property Tomography (MR- EPT)  
for Prostate Cancer Grade Imaging

PRINCIPAL INVESTIGATOR: Ryan Halter

CONTRACTING ORGANIZATION: Dartmouth College  
Hanover, NH 03755-4099

REPORT DATE: July 2016

TYPE OF REPORT: Annual

PREPARED FOR: U.S. Army Medical Research and Materiel Command  
Fort Detrick, Maryland 21702-5012

DISTRIBUTION STATEMENT: Approved for Public Release;  
Distribution Unlimited

The views, opinions and/or findings contained in this report are those of the author(s) and should not be construed as an official Department of the Army position, policy or decision unless so designated by other documentation.

<b>REPORT DOCUMENTATION PAGE</b>				Form Approved OMB No. 0704-0188	
Public reporting burden for this collection of information is estimated to average 1 hour per response, including the time for reviewing instructions, searching existing data sources, gathering and maintaining the data needed, and completing and reviewing this collection of information. Send comments regarding this burden estimate or any other aspect of this collection of information, including suggestions for reducing this burden to Department of Defense, Washington Headquarters Services, Directorate for Information Operations and Reports (0704-0188), 1215 Jefferson Davis Highway, Suite 1204, Arlington, VA 22202-4302. Respondents should be aware that notwithstanding any other provision of law, no person shall be subject to any penalty for failing to comply with a collection of information if it does not display a currently valid OMB control number. <b>PLEASE DO NOT RETURN YOUR FORM TO THE ABOVE ADDRESS.</b>					
<b>1. REPORT DATE</b> July 2016		<b>2. REPORT TYPE</b> Annual		<b>3. DATES COVERED</b> July 1, 2015 – June 30, 2016	
<b>4. TITLE AND SUBTITLE</b>  Magnetic Resonance-Based Electrical Property Tomography (MR- EPT) for Prostate Cancer Grade Imaging				<b>5a. CONTRACT NUMBER</b> W81XWH-13-1-0127	
				<b>5b. GRANT NUMBER</b> PC120904	
				<b>5c. PROGRAM ELEMENT NUMBER</b>	
<b>6. AUTHOR(S)</b> Ryan Halter  E-Mail: ryan.halter@dartmouth.edu				<b>5d. PROJECT NUMBER</b>	
				<b>5e. TASK NUMBER</b>	
				<b>5f. WORK UNIT NUMBER</b>	
<b>7. PERFORMING ORGANIZATION NAME(S) AND ADDRESS(ES)</b> Dartmouth College Office of Sponsored Projects 11 Rope Ferry Road #6210 Hanover, NH 03755-1404				<b>8. PERFORMING ORGANIZATION REPORT NUMBER</b>	
<b>9. SPONSORING / MONITORING AGENCY NAME(S) AND ADDRESS(ES)</b> U.S. Army Medical Research and Materiel Command Fort Detrick, Maryland 21702-5012				<b>10. SPONSOR/MONITOR'S ACRONYM(S)</b>	
				<b>11. SPONSOR/MONITOR'S REPORT NUMBER(S)</b>	
<b>12. DISTRIBUTION / AVAILABILITY STATEMENT</b> Approved for Public Release; Distribution Unlimited					
<b>13. SUPPLEMENTARY NOTES</b>					
<b>14. ABSTRACT</b> Determining whether a man recently diagnosed with prostate cancer has aggressive disease requiring immediately radical therapy or indolent disease requiring a more passive watchful waiting or active surveillance approach is a current clinical challenge. This technology development study is focused on developing Magnetic Resonance – Electrical Property Tomography (MR-EPT) specifically for prostate imaging. MR-EPT is an imaging modality that may enable clinicians to image the electrical properties of prostate at near MR resolution. These electrical properties are hypothesized to provide sufficient contrast for distinguishing between aggressive and indolent prostate cancer. Much of the third year of this program has focused on additional MR-EPT image reconstruction algorithm development and optimization, experimental imaging of both simplistic and anatomically accurate phantoms, continued recruitment for ex vivo and in vivo prostate imaging, and statistical analysis of ex vivo prostate data. During this year we have demonstrated additional imaging capabilities of MR-EPT through phantom studies, have recruited and imaged the majority of our proposed ex vivo cohort of prostates, and continued recruitment for the in vivo imaging phase of this program. The no-cost-extension 6 months of the program will primarily focus on completing our in vivo data acquisition, statistical analysis of our data, and preparation of publications and proposals for follow-on more clinically focused studies.					
<b>15. SUBJECT TERMS</b> Nothing listed					
<b>16. SECURITY CLASSIFICATION OF:</b>			<b>17. LIMITATION OF ABSTRACT</b>  UU	<b>18. NUMBER OF PAGES</b>  24	<b>19a. NAME OF RESPONSIBLE PERSON</b> USAMRMC
<b>a. REPORT</b> U	<b>b. ABSTRACT</b> U	<b>c. THIS PAGE</b> U			<b>19b. TELEPHONE NUMBER</b> (include area code)

Table of Contents

	<u>Page</u>
Introduction.....	2
Body.....	2
Key Research Accomplishments.....	8
Reportable Outcomes.....	8
Conclusion.....	8
Appendices.....	9
Appendix 1: IEEE TMI Draft.....	10

## INTRODUCTION

This program builds off of our extensive experience in using electrical properties of prostate to distinguish malignant from benign tissues [1-5] and specifically stems from exciting new data published in The Prostate [6] in which we demonstrated significant electrical property differences between high- and low-grade prostate cancer. These electrical properties are influenced by a tissue's intra- and extra-cellular composition, morphology, and cellular constituency, and we have hypothesize that it is possible to use these properties to discriminate between normal, low-grade, and high-grade malignant formations in a clinical setting. While measuring these properties by direct contact with the tissues is possible in invasive experiments, it is desirable to develop methods to do so in a non-invasive fashion. To date our group, and other groups around the world, have investigated Electrical Impedance Tomography and Microwave Imaging, two techniques which are limited in resolution by the underlying physics. The primary objective of this current program is to develop a high-resolution MR-based approach to imaging the electrical properties of prostate with the intent of producing a system potentially able to image cancer grade. This is possible by leveraging ultra-novel developments in MRI, and our extensive experience in developing technologies to gauge and assess the utility of electrical properties for prostate cancer detection [1-6] and assessment and in developing computer algorithms to transform electromagnetic data into electrical property images of the prostate [7-14]. Specifically, we are attempting to use the maps of MRI RF field data acquired with safe and fast sequences to create high-resolution electrical property images of the prostate. We are developing this novel technology, evaluating it in an *ex vivo* setting, and finally assessing the feasibility of employing this imaging modality in a routine clinical cohort of patients with the intent of having a significant and immediate impact on clinical practice. By developing this high-resolution electrical property imaging modality we expect to produce highly sensitive and specific images of cancer grade within the prostate and ultimately better guide clinicians in distinguishing aggressive from indolent disease.

Much of the third year of this program has focused on *ex vivo* prostate imaging, *ex vivo* data analysis, continued developing of MR-EPT conductivity reconstructions, and initiation of *in vivo* data collections. We are currently in a No Cost Extension period (additional 6 months) in which we will focus on completing the *in vivo* data collection and statistical analysis of our data. In addition we will be preparing publications and proposals focused more heavily on clinical data acquisition and evaluation.

## BODY

The following research summary is presented in terms of the approved Statement of Work, with each task being discussed separately. When appropriate, detailed discussion is referenced to manuscripts published, submitted, or in preparation which are provided in the Appendix. Information provided in our previous annual report is omitted here and instead we note the tasks that are completed and reference our 2014/2015 annual reports. Note that future task and objectives to be completed are marked as **TBC**.

### **SPECIFIC AIM 1: TO DEVELOP MR-EPT FOR PROSTATE IMAGING**

#### **Major Task 1: Develop computation toolbox for MR-EPT**

##### a) Build Matlab-based toolbox for computing electrical property images

*Completed and reported on in our 2014/2015 Annual Reports. On-going investigation continue in order to further optimize and validate the approach developed.*

*We have fully implemented our proposed method as a MATLAB toolbox for MR-EPT image reconstruction as described in our 2014/2015 annual reports. Over the past year we made two significant advancements. The first is a method for smoothing the boundaries between sub-domains within our images and the second is a method for reconstructing permittivity of an object. In terms of smoothing out the sub-domains, we have developed an overlapping method by which we reconstruct conductivity over multiple overlapping sub-domains of different sizes. By properly accounting for the overlapping pixels we can average these sub-domains together and smooth out the boundaries between the sub-domains. This creates significantly more appealing images that do not have sharp transitions between the different sub-domains (as were present in our previous implementations). Figure 1 depicts the process and Figure 2 demonstrates the significant image quality improvements achievable with this optimized algorithm.*

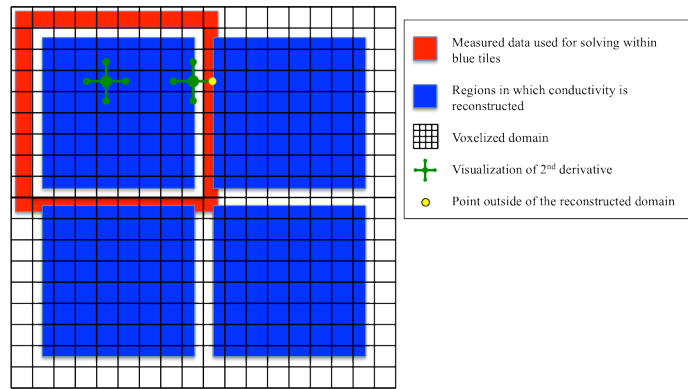


Figure 1. Illustration of the tiling subdomains, data used in reconstructing (red square), and a 2<sup>nd</sup> derivative smoothing constrain.

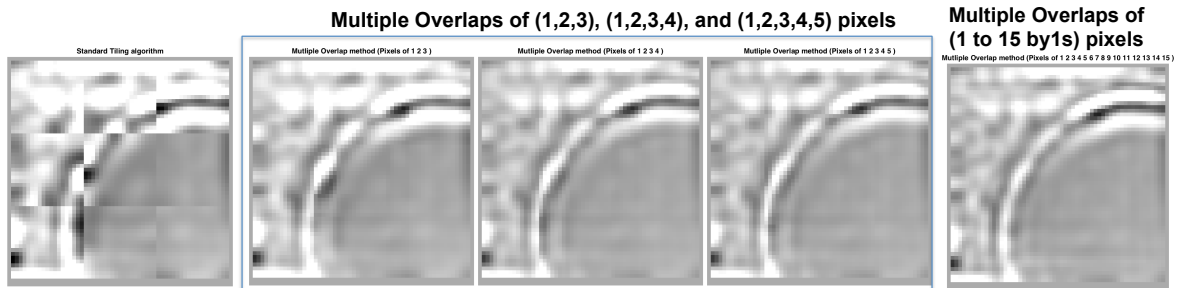


Figure 2: Several examples of multiple overlays used to smooth the internal boundary artifacts. Note that the image on the left was our initial implementation and that the internal artifacts are significantly reduced as we average over multiple overlays

In terms of permittivity imaging, we have developed a forward model, the Jacobian, and an iterative approach to estimating the permittivity distribution. We have evaluated this in simulation and plan to evaluate this in phantom models during the next quarter. Figure 3 shows an example image of permittivity reconstruction and a PowerPoint presentation describing this development is appended to this quarterly report.

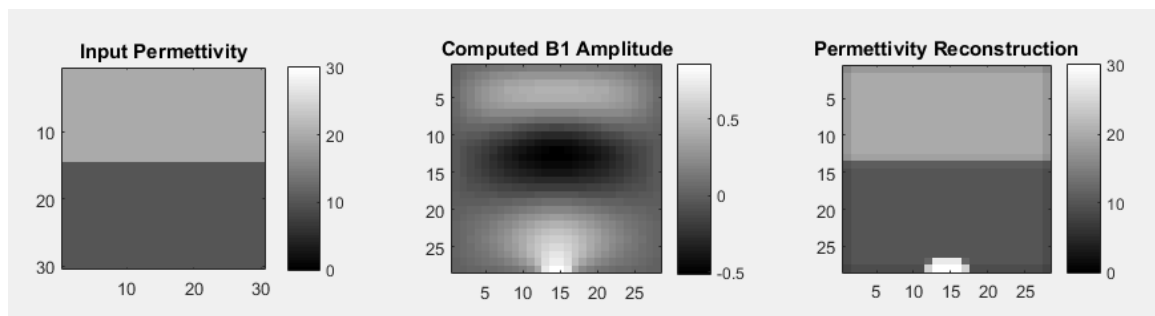


Figure 3: Example simulation of permittivity reconstruction. Left image is true permittivity distribution. Central image represents the B1 amplitude map computed with our forward solver. Right image represents the reconstructed permittivity. Note that the reconstructed permittivity closely matches the true permittivity distribution (left image), with the exception of a few boundary pixels which are artificially elevated due to how the boundary conditions are implemented to solve the forward problem.

- b) Build Matlab-based toolbox for specific MR-based field of views  
Completed and reported on in our 2014/2015 Annual Reports. On-going investigation/developments continue in order to further optimize and validate this toolbox.

We have developed Matlab-based functions to read in arbitrary MRI DICOM and .PAR/.REC (Phillips format) images and display them for evaluation. Additional developments have included the ability to create multi-slice images of the MR data for use in comparing the different MR variants we are exploring. This toolbox was briefly described in our 2014/2015 annual reports.

#### Task 1 Milestones:

1. Functional toolbox for producing MR-EPT images – **Completed**

## **Major Task 2: Optimize MR-EPT and multi-parametric MR imaging through phantom imaging**

### **a) Optimize MR-sequence for MR-EPT**

*Completed and reported on in our 2014/2015 Annual Reports.*

### **b) Perform initial tank-based phantom imaging studies**

*Completed and reported on in our 2014/2015 Annual Reports. On-going investigation continue in order to further optimize and validate the approach developed.*

*A number of additional tank-based phantom studies were conducted during this past year to further demonstrate that our MR-EPT algorithms are able to accurately estimate the internal conductivity of a volume. One such experiment specifically focused on... validating that our approach is able to accurately reconstruct curved surfaces (some of our previous experiments explored linearly varying conductivity changes). Figure 2 displays a curvilinear gelatin phantom conducted along with the MR magnitude image produced. The phase data recorded from this experiment was reconstructed using both QR and TV approaches to solve the inverse problem (Figure 3). Both approaches accurately reconstruct the curved surface suggesting that these techniques extend beyond reconstructing linearly varying conductivity distributions. In addition, we divide the phase images into a number of sub-domains to reduce the computational time associated with image reconstruction. We explored this and the time associated with using different numbers of sub-domains (Figure 3 and Table 1). The experimental configuration and analysis are further described in Appendix 1.*

### **c) Perform anatomically accurate phantom imaging studies**

*Completed and reported on in our 2014/2015 Annual Reports.*

## **Task 2 Milestones:**

*Note that while the below tasks are complete, we expect to continue conducting phantom experiments over the course of the next year to continue to improve our image reconstruction algorithms and better understand any image artifacts that may appear in our clinical data acquisition.*

1. Validated MR-EPT algorithms – **Completed**
2. Fully functional protocol for obtaining MR-based images in a single serially acquired imaging session – **Completed**
3. 1 peer-reviewed publication submitted – **Completed, see Appendix**

## **Major Task 3: Submit documents for IRB and MRMC HRPO approval**

### **a) Draft and submit IRB protocol revisions and new protocol submission**

**Ex vivo Protocol:** *Completed during last annual reporting period.*

**In Vivo Protocol:** *Completed during last annual reporting period*

### **b) Draft and submit documentation for MRMC HRPO approval**

**Ex vivo Protocol:** *Completed during last annual reporting period*

**In Vivo Protocol:** *Completed during last annual reporting period*

## **Task 3 Milestones:**

1. Obtain IRB and MRMC HRPO approval for ex vivo and in vivo cohorts – **ex vivo completed, in vivo completed**

## **SPECIFIC AIM 2: TO EVALUATE MR-EPT IN AN EX VIVO COHORT OF PROSTATES**

## **Major Task 1: Optimize ex vivo MR-EPT and multi-parametric MR imaging**

### **a) Record MR-EPT and multi-parametric MR sequences of ex vivo prostates**

*This task has been complete and described in our 2014/2015 Annual Reports.*

### **b) Optimize MR-EPT sequences and algorithms based on findings in this initial cohort**

*This task has been complete and described in our 2014/2015 Annual Reports.*

### Task 1 Milestones:

1. Validation that our MR-EPT and multi-parametric MR protocol is initially optimized, robust, and repeatable – **Completed**

### Major Task 2: Evaluate ex vivo MR-EPT and multi-parametric MR imaging

- a) Record multi-parametric MR sequences of ex vivo prostates

*Over the past year we have actively recruited patients to participate in our ex vivo study. We have been averaging ~ 2 cases per month. To date we have imaged 50 ex vivo prostates (reaching our target accrual). For all cases we have been recording B1 phase and magnitude images (for MR-EPT image reconstruction), T1 spin echo, T1 turbo spin echo, and T2 turbo spin echo images. – Completed*

- b) Perform semi-quantitative and quantitative analysis of ex vivo prostate samples

*We reported on an interim statistical analysis during our last annual report. We just finished accruing data from our final ex vivo patients this past month and are in the process of compiling a final statistical assessment of our ex vivo data. This will be completed by the end of this current NCE period.*

- c) Statistically analyze MR-based images and pathological metrics

*Data generation continues to be in process (MR images & Pathology metrics). Figure 4 shows a typical panel of images we create for each prostate imaged. We also have the ability to produce a variety of MR-EPT images based on different algorithms we developed (and described in previous reports) (Fig 5). We have fully reconstructed 47 of our 50 cases.*

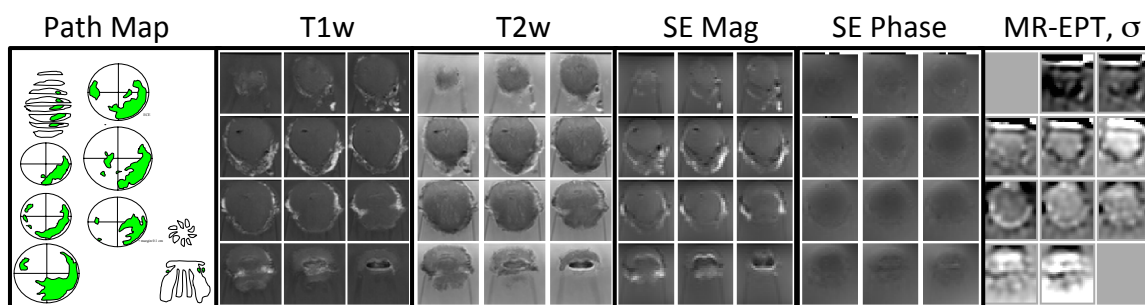


Figure 4: Typical panel of data images recorded and to be used for statistical analysis.  $\sigma$  denotes conductivity images.

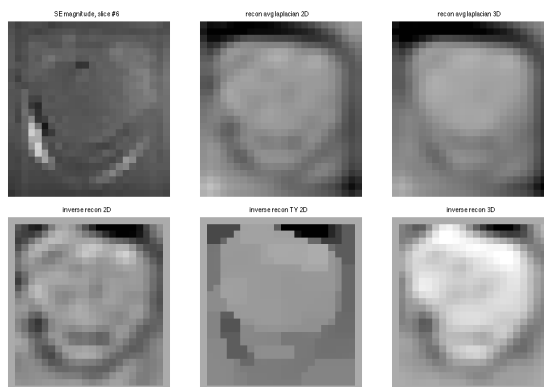


Figure 5. Typical panel of conductivity images based on applying different MR-EPT algorithms we have developed. This particular example displays a single slice from a patient. Five different reconstruction algorithms (discussed in previous reports) were used to produce these conductivity images. We plan to statistically analyze each of the algorithms when evaluating the clinical efficacy of MR-EPT.

### Task 2 Milestones:

1. Assessment of the clinical potential MR-EPT combined with multi-parametric MR might have for prostate imaging – **in process (TBC)**
2. 1 peer-reviewed publication submitted – **in process (TBC)**

### **SPECIFIC AIM 3: TO EVALUATE MR-EPT IN AN IN VIVO COHORT OF PATIENTS**

#### **Major Task 1: Evaluate *in vivo* MR-EPT and multi-parametric MR imaging**

- a) Record MR-EPT and multi-parametric MR sequences of *in vivo* and *ex vivo* prostates

*Recruiting patients for our in vivo protocol is in progress. We have enrolled 5 men into our in vivo protocol. We have conducted an initial analysis of our in vivo data and have noted that there are significant image artifacts that are present. This may be due to a phase wrapping issue or a low signal issue associated with the much larger field of view that we are trying to image. The figure on the right shows an example series of phase images acquired of a man's prostate. The individual images correspond to an image stack. The unsmooth variation in the images are not expected nor observed in ex vivo and small phantom imaging.*

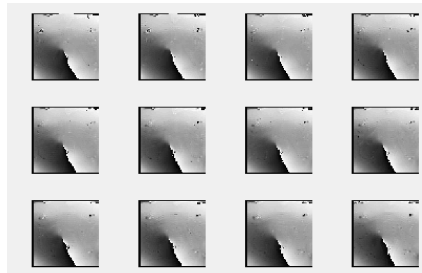


**Figure 6.** *In vivo* series of prostate phase images acquired from a volunteer. Note the significant phase-wrapping artifact present in these images. This artifact produced MR-EPT conductivity images with severe artifacts.

*To determine if this is due to the large field of view or to the tissue being sampled in vivo we recorded data from a volunteer's calf. Note the phase images on the right do not show the significant artifact present in the in vivo phase images of the prostate. Further, the conductivity images derived from these phase images clearly show the outer adipose layer and the tibia and fibula bones within the calf musculature. We are in the process of evaluating large saline tanks to determine how the field-of-view influences the acquired phase images.*

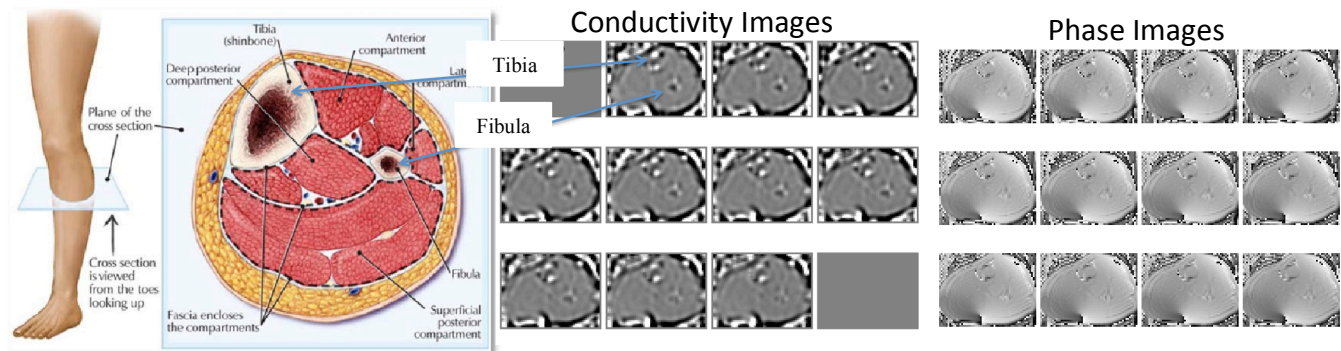


**Figure 7.** *In vivo* series of calf images. Note that the phase images do not suffer from the same phase wrapping artifact present within the in vivo prostate images. The conductivity images (center panel) were successfully reconstructed from these phase images and clearly show the low conductivity tibia and fibula.

*We have conducted larger phantom tests with this MR bore to better simulate in vivo conditions. Specifically, we created gel phantoms in a 5-gallon bucket. The phantom ended up consisting of a gelatin cylinder ~12" in diameter and 12" in height. A gelatin prostate with copper sulfate (MR contrast) and additional salt (to provide conductivity contrast) was formed. A plastic (low conductivity) bead was placed within the prostate to emulate a tumor. Note that this study was carried out specifically to try to explore the phase artifacts we observed in the in vivo cases. We showed with this phantom that the phase images are artifact free if we set the appropriate field of view.*

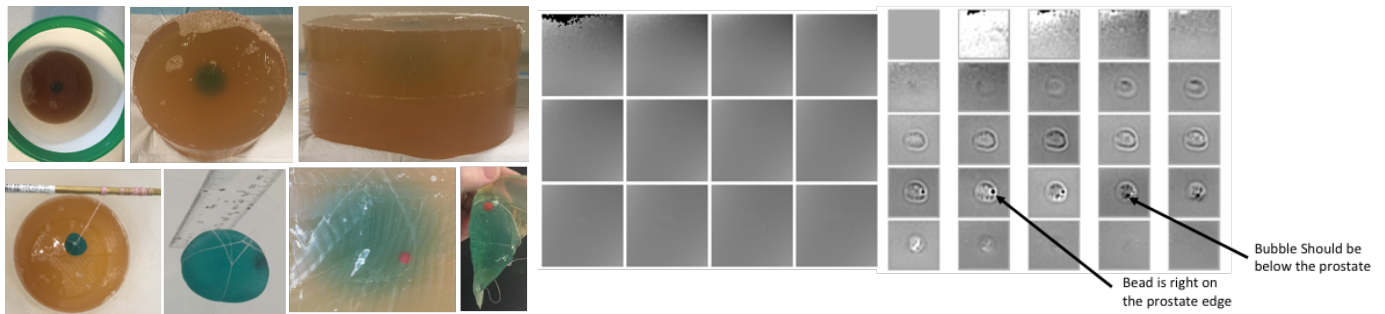


**Figure 8.** Large gel phantom used to better simulate in vivo images conditions. A large cylindrical gel phantom was created; a smaller anatomically accurate gel prostate with a bead inserted (to simulate a tumor) was embedded within the large cylindrical gel phantom (left panels). The phase images acquired show a very uniform phase distribution with no phase wrapping (central panels). The reconstructed MR-EPT conductivity images clearly show the prostate, tumor, and a small air bubble that was trapped in the phantom during fabrication. This experiment was used to explore several field of views (FOVs) and imaging directions within the bore. The optimal FOV used a large region in which the coil was positioned Anterior to Posterior and the phase direction was oriented from left to right.

Based on these results we conducted addition in vivo tests on a normal volunteer to see if changing the FOV helped to minimize phase artifacts and enable MR-EPT reconstruction of conductivity images. We explored a number of different FOVs and imaging directions (see Table). Figure 10 shows example magnitude and phase images acquired of a volunteer using the FOVs and directions specified in the above table. Note that the phase images do not have the wrapping artifact that was present in our earlier phase images of in vivo prostate (see above). We have reconstructed these images to produce the first ever in vivo MR-EPT images of prostate (Figure 11).

Series	Field of View	Coil	Phase
4	Small	Left & Anterior	Anterior & Posterior
6	Large	Left & Anterior	Anterior & Posterior
9	Small	Anterior & Posterior	Left & Right
11	Large	Anterior & Posterior	Left & Right

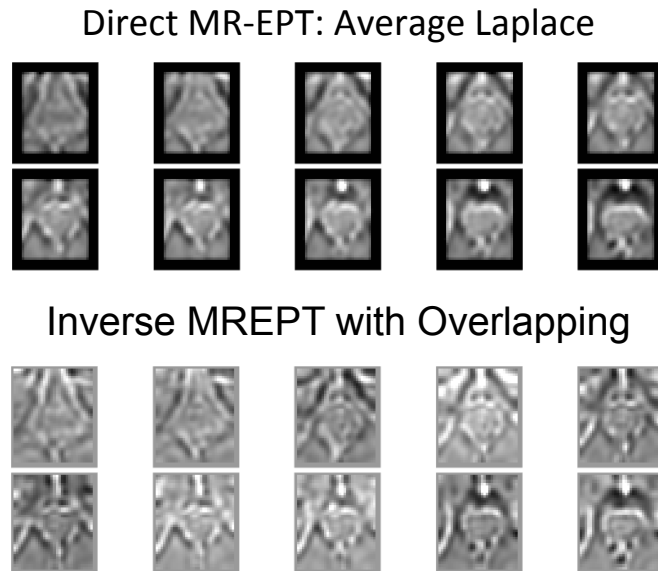


**Figure 10.** In vivo series of MR-EPT prostate conductivity images acquired from a volunteer. These represent the first ever in vivo conductivity images computed using MR-EPT of the prostate. Two different reconstruction approaches are presented here: the direct average Laplace approach and our inverse approach using our newly implemented overlapping strategy to smooth internal boundaries. Both panels of images clearly show the prostate with a somewhat heterogeneous intraprostatic region and a low conductivity peri-prostatic region. This approach will be used for image acquisition and reconstruction in our remaining in vivo

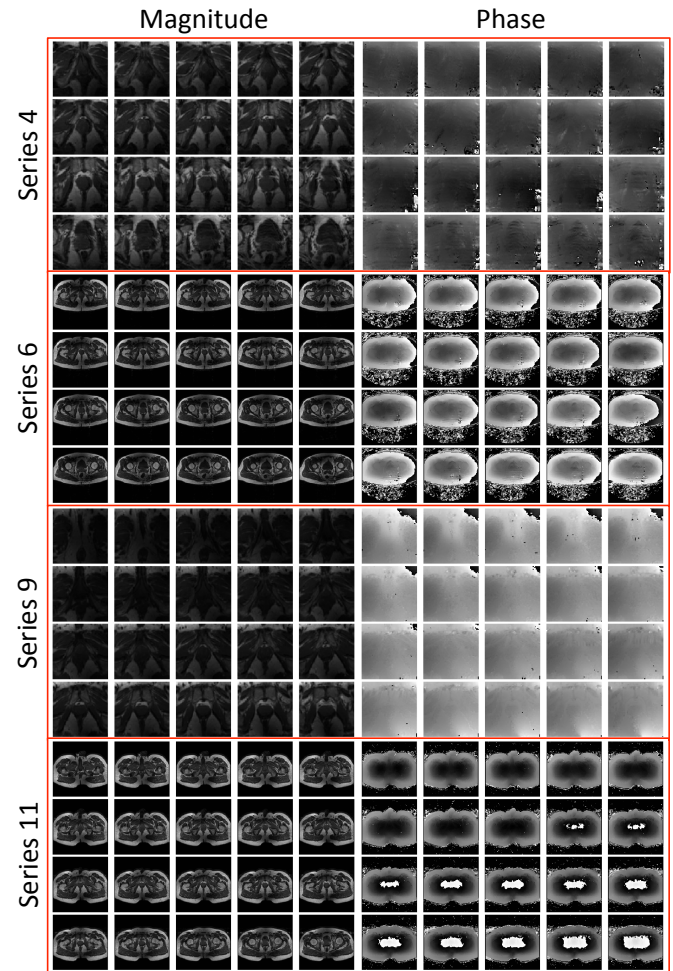


**Figure 9.** In vivo series of prostate images acquired from a volunteer. These panels show the magnitude (left) and phase (right) images acquired using the different FOVs, coil and phase directions as specified in the above table. Note that the phase wrapping present in Series 11 was easily unwrapped since it was somewhat continuous in the angular direction. Series 11 provided the best conductivity images (see Fig 11).

- b) Perform post-prostatectomy pathological assessment of extracted prostates  
*To be completed during the remaining NCE period of this program*
- c) Statistically analyze MR-based images and pathological metrics  
*To be completed during the remaining NCE period of this program*

**Task 1 Milestones:**

1. Comparison between in vivo and ex vivo MR-EPT – **TBC**
2. Preliminary clinical statistics defining utility of MR-EPT combined with other MR-imaging variants – **TBC**
3. Initial parameter threshold values for use in detecting and staging prostate cancer – **TBC**
4. 1 peer-reviewed publication submitted – **TBC**

**KEY RESEARCH ACCOMPLISHMENTS**

- Assembled a database of MR and MR-EPT images from 50 ex vivo human prostate samples; this will ultimately be made available to the research community once we have completed statistical analysis of this database.
- Developed a novel overlapping scheme that enables us to produce MR-EPT conductivity images with no internal boundary artifacts.
- Developed MR-EPT permittivity imaging using an inverse approach similar to what we developed for use in conductivity imaging.
- Produced the first ever MR-EPT-based conductivity images of in vivo human prostate that clearly shows the prostate

**REPORTABLE OUTCOMES**

***Manuscripts***

Borsic A, Perreard I, Mahara A, Halter RJ, “An Inverse Problems Approach to MR-EPT Image Reconstruction,” IEEE Transactions on Medical Imaging, accepted with minor modifications June 2015. (**Appendix 1 – published manuscript**)

Perreard I, Borsic A, Mahara A, Halter RJ, “Towards Magnetic Resonance – Electrical Properties Tomography (MR-EPT) for Prostate Imaging,” Medical Physics, to be submitted September 2016 (**draft in progress**)

**CONCLUSION**

It is a daily challenge for clinicians to determine whether a man recently diagnosed with prostate cancer has aggressive disease requiring immediately radical therapy or indolent disease requiring a more passive watchful waiting or active surveillance approach. This program is focused on developing Magnetic Resonance – Electrical Property Tomography (MR-EPT) specifically for prostate imaging. Over the past year we have continued to optimize our MR-EPT algorithms for estimating the prostate’s electrical conductivity given magnetic field phase and magnitude images acquired using custom MR sequences. We have conducted a series of experiments to demonstrate that in vivo prostate imaging is possible. Additional simulations and phantom experiments have been conducted to explore the influence of field-of-view, coil position, and phase direction have on our MR-EPT images and to validate that we can image in vivo objects with dimension similar to those expected in human imaging. We have completed enrollment of our ex vivo study (have recorded data from 50 ex vivo prostates) and are currently in the process of performing a final statistical assessment of this data. Finally, the first ever in vivo prostate conductivity images that clearly show the prostate and surrounding tissues were generated using MR-EPT. Over the course of the final NCE period, we will be focusing primarily on clinical data acquisition (in vivo cohorts) and in analyzing images acquired to assess the potential of using MR-EPT (coupled with other MR imaging variants) to distinguish between aggressive and indolent prostate cancer.

## **APPENDICES**

### **Appendix 1: IEEE TMI Published Manuscript**

# An Inverse Problems Approach to MR-EPT Image Reconstruction

A. Borsic\*, I. Perreard, A. Mahara, and R. J. Halter

**Abstract**—Magnetic Resonance—Electrical Properties Tomography (MR-EPT) is an imaging modality that maps the spatial distribution of the electrical conductivity and permittivity using standard MRI systems. The presence of a body within the scanner alters the RF field, and by mapping these alterations it is possible to recover the electrical properties. The field is time-harmonic, and can be described by the Helmholtz equation. Approximations to this equation have been previously used to estimate conductivity and permittivity in terms of first or second derivatives of RF field data. Using these same approximations, an inverse approach to solving the MR-EPT problem is presented here that leverages a forward model for describing the magnitude and phase of the field within the imaging domain, and a fitting approach for estimating the electrical properties distribution. The advantages of this approach are that 1) differentiation of the measured data is not required, thus reducing noise sensitivity, and 2) different regularization schemes can be adopted, depending on prior knowledge of the distribution of conductivity or permittivity, leading to improved image quality. To demonstrate the developed approach, both Quadratic (QR) and Total Variation (TV) regularization methods were implemented and evaluated through numerical simulation and experimentally acquired data. The proposed inverse approach to MR-EPT reconstruction correctly identifies contrasts and accurately reconstructs the geometry in both simulations and experiments. The TV regularized scheme reconstructs sharp spatial transitions, which are difficult to reconstruct with other, more traditional approaches.

**Index Terms**—Conductivity, electrical properties tomography, inverse problem, magnetic resonance, permittivity, primal dual—interior point method, quadratic regularization, reconstruction, total variation regularization.

## I. INTRODUCTION

**M**AGNETIC RESONANCE-ELECTRICAL PROPERTIES TOMOGRAPHY (MR-EPT) is an imaging modality that maps the spatial distribution of the electrical conductivity and permittivity using standard clinical MR systems. This technique exploits  $B_1$  field perturbations associated with the objects present within the bore of the scanner. These field

perturbations can be used to estimate the spatial distribution of electrical properties within the objects giving rise to the perturbations.

Early work in MR-EPT was published in 1991 [1], but the technique has only recently seen a resurgence of exploration due to the clinical potential that the electrical properties may offer in terms of tissue contrast. Several groups have focused on developing novel image reconstruction methods and algorithms for this purpose.

Reconstruction algorithms can be classified as *direct methods*, from which measured  $B_1$  information is directly used to map the electrical properties (EPs), and as *inverse methods*, in which EPs are estimated by fitting a model to the measured data. The initial work by Haake *et al.* [1] is based on using the Helmholtz equation for describing the time harmonic magnetic field  $\vec{H}$  at radio frequencies used in MRI imaging:

$$\nabla^2 \vec{H} = -\mu\omega^2 k \vec{H} + \left[ \frac{\nabla k}{k} \times (\nabla \times \vec{H}) \right] \quad (1)$$

where  $k = \epsilon - j(\sigma/\omega)$ , and  $\omega$  is the angular frequency of the  $\vec{H}$  field,  $\sigma$  the electrical conductivity,  $\epsilon$  the electrical permittivity, and  $\mu$  the magnetic permeability. Assuming that  $\sigma$  and  $\epsilon$  are piecewise constant or slowly varying (i.e.  $\nabla k \approx 0$ ), the second term on the right hand side of (1) can be neglected. Considering only the MRI-measurable positive circularly polarized component  $H^+$  of the RF transmit field, and considering  $k$  as isotropic, one obtains:

$$k = \frac{-1}{\mu\omega^2} \frac{\nabla^2 H^+}{H^+} \quad (2)$$

which expresses the EPs as a function of the  $H^+$  field and its second derivative. One method for measuring  $H^+$  amplitude is through use of double—angle mapping techniques [2],  $H^+$  phase is assumed to be half of the spin—echo phase, an assumption valid when one transmit and one receive coil are used, and the sensitivity patterns of the two coils have a similar spatial distribution but a reverse polarity [3]. Typically, in biological tissues,  $\mu$  is considered equal to the permeability of free space  $\mu_0$ .

Despite the simplifying assumptions (2), this approach has successfully been used to fit layered models [1] and to produce electrical properties images in post-mortem animals [4]. While this approach is feasible, the 2nd-order differentiation required for computing the Laplacian is sensitive to noise, and therefore not desirable. In 2009, Katscher *et al.* [3] used the Gauss theorem to propose an alternate formulation that decreases the differentiation from 2nd to 1st order. With this transformation, the

Manuscript received July 07, 2015; revised July 27, 2015; accepted August 03, 2015. Date of publication August 20, 2015; date of current version December 29, 2015. Asterisk indicates corresponding author.

\*A. Borsic is with NE Scientific LLC, Lebanon, NH 03766 USA (e-mail: aborsic@ne-scientific.com).

I. Perreard is with the Department of Radiology, Dartmouth Hitchcock Medical Center, Dartmouth College, Lebanon, NH 03766 USA.

A. Mahara and R. J. Halter are with the Thayer School of Engineering, Dartmouth College, Hanover, NH 03755 USA.

Color versions of one or more of the figures in this paper are available online at <http://ieeexplore.ieee.org>.

Digital Object Identifier 10.1109/TMI.2015.2466082

conductivity and permittivity are proportional to surface integrals of the gradient of  $H^+$  phase and amplitude, over the surface of an arbitrary block of pixels where the electrical properties are assumed to be approximately constant. This approach has been successfully demonstrated in in-vitro and in in-vivo experiments [3], [5], [6] and exhibits decreased noise sensitivity compared to previously considered approaches.

The assumption that EPs are constant or slowly varying also does not broadly apply to imaging of biological tissues, and the errors arising from violating this assumption are analyzed in detail by Seo *et al.* [7].

An approach based on measuring two sets of  $H^+$  data with multi-channel MRI systems was proposed by Zhang *et al.* [8]. This approach reduces artifacts resulting from fast spatial variations of EPs, but requires measuring components of  $H^+$  in the  $(x, y)$  plane of the scanner, which is impractical in clinical applications, where only the  $z$  component along the direction of the static magnetic field is normally available.

Sodickson *et al.* [9] derived a general formulation to MR-EPT that does not make assumptions on the distribution of EPs and that is suitable for multi-channel systems. In this approach conductivity, permittivity, phase, phase derivatives, magnetization, and magnetization derivatives are assumed to be unknowns. This approach has produced promising numerical results, however, it requires computing spatially-dependent second derivatives and may therefore be sensitive to noise in experimental applications. An approach based on formulating the dependence of EPs on  $H^+$  via the convection—reaction equation has been developed by Hafalir *et al.* [10]. This approach does not make any restrictive assumption on the distribution of EPs. However, this method also requires first and second derivatives of  $H^+$  be computed and is therefore potentially sensitive to noise; despite this, it has been demonstrated numerically and experimentally to provide results that are superior to standard methods based on (2).

Inverse approaches to MR-EPT have been also considered. An algorithm termed CSI-EPT (Contrast Source Inversion-EPT) has been proposed by Balidemaj *et al.* [11]. This algorithm does not make any assumption regarding the distribution of EPs and is based on an inverse formulation, where the EPs are fit to the data using a contrast source approach. The method has been shown in numerical simulations to produce accurate and detailed reconstructions of a pelvis model. Total Variation [12] regularization has also been adopted in order to reduce this method's sensitivity to noise. To the best of our knowledge this method has not yet been demonstrated on experimental data. A model—based approach to conductivity reconstruction which incorporates regularization techniques has also been proposed by Ropella *et al.* [13]. This approach is based on inverting the Laplacian in (3) in the Fourier domain, and has demonstrated better image quality compared to traditional direct approaches in phantoms and in in-vivo data.

In this manuscript we present a novel MR-EPT reconstruction algorithm resulting from further development and enhancement of initial work developed by the authors [14], [15]. The algorithm is based on an inverse approach applied to (2). Conductivity and permittivity are treated separately as in [4], and

taken as parameters to be fitted. A forward model is developed to link electrical parameters to the  $H^+$  data. A Jacobian matrix, based on the forward model, is defined and used for updating the model parameters. Regularization is used to stabilize the inversion for parameter estimation. This inverse approach to MR-EPT, based on fitting  $H^+$  data with a model, has the general advantage compared to direct methods based on (2), and with respect to [9], [10], of not requiring differentiation of measured  $H^+$  data, and is therefore less sensitive to noise. The approach is demonstrated to successfully reconstruct noisy numerical and experimental data. Because this approach casts MR-EPT reconstruction in a well established inverse problem framework, two well known regularization techniques, Quadratic Regularization and Total Variation regularization are implemented to reduce the effects of noise and to stabilize the inversion. Quadratic Regularization leads to smoother reconstructed images, while Total Variation regularization is able to produce sharper images. This method, being based on the approximate relationship (2), which might result in artifacts at the interface of highly enterogenous boundaries as discussed in [7]. However, this approach is common in MR-EPT, and has been demonstrated to produce meaningful images [3], [5], [6], [16], [17].

Algorithms based on (2) have been applied to breast cancer detection, showing potential of MR-EPT as a diagnostic tool. In this context prior structural information available from T1 and/or T2 weighted MRI imaging has been used to enhance the reconstructed EPs by weighting differently variations along the normal and tangential direction with respect to the expected prior features [16], [17]. Our approach also enables incorporating prior structural information, so that preferential directions of change of EP can be embedded into the regularization (e.g. [18], [19]). In general we believe that the approach developed here has advantages over algorithms based directly on (2) since it does not require differentiation of  $H^+$ . This may make it more suitable for clinical applications where noise is present. It is difficult to offer comparative remarks with respect to recent inverse algorithms [9]–[11], as these comparisons will likely require application of the different algorithms on particular tests cases.

Reconstruction of EPs with the inverse approach developed here entails considering the EPs of every pixel in the image as an unknown to be estimated. For three-dimensional datasets this can result in an excessive computational burden. We describe methods for splitting the imaging domain that significantly reduce this burden.

In Section II we introduce our reconstruction approach and develop a forward model. In Section III we describe an inverse formulation for reconstructing EPs, and in Section IV we discuss an implementation using Quadratic Regularization and one using Total Variation regularization. Section V reports numerical experiments, Section VI discusses the computational burden of the methods developed and offers methods for reducing it, Section VII reports image reconstruction results from physical experiments. Finally concluding remarks are offered.

## II. FORWARD MODEL

The MR-EPT reconstruction approach developed here is based on an inverse formulation, in which a model is fit to measured data. In this context, the relationship linking the  $H^+$  field

data to the electrical conductivity,  $\sigma$ , and permittivity,  $\epsilon$ , defines the forward model. These relationships can be approximated as [4]:

$$\sigma = \frac{1}{\mu_0 \omega} \nabla^2 \phi(H^+) \quad (3)$$

and

$$\epsilon = -\frac{1}{\mu_0 \omega^2} \frac{\nabla^2 |H^+|}{|H^+|} \quad (4)$$

Equation (3) can be recognized as the Poisson equation:

$$\nabla^2 \phi = \mu_0 \omega \sigma \quad (5)$$

where for simplicity  $\phi$  denotes  $\phi(H^+)$ . Equation (4) takes the form of the Helmholtz equation:

$$\nabla^2 \Lambda + \mu_0 \omega^2 \epsilon \Lambda = 0 \quad (6)$$

where for simplicity  $\Lambda$  denotes  $|H^+|$ .

This manuscript focuses on reconstructing conductivity from (5). Permittivity can be reconstructed from (6) with similar methods, which are not developed in this manuscript. Boundary conditions appropriate to the physics describing the forward model need to be specified in order to solve (5). This approach ultimately aims to match a measured phase  $\phi_{meas}$  with a simulated  $\phi$  computed from (5); Dirichlet conditions defining the phase on the domain boundary are therefore ideal for this case. This conditions is specified as

$$\phi(r) = \phi(r)_{meas} \quad \forall r \in \partial\Omega \quad (7)$$

where  $r$  is a point in space and  $\partial\Omega$  is the boundary of the imaging domain.  $\phi_{meas}$  is perfectly matched at the boundary through use of (7), and it will be matched point-by-point inside the domain by appropriate adjustment of the  $\sigma$  distribution. It is worth noting that for any value of measured data,  $\phi_{meas}$ , the condition (7) is compatible with (5) [20], and therefore a solution to (5) always exists and is unique for those boundary conditions [20]. Equations (5) and (7) define a forward model for MR-EPT conductivity reconstruction via the inverse approach developed here.

### III. INVERSE FORMULATION

The forward model linking  $\phi$  to  $\sigma$  can be used to establish an estimate of the  $\sigma$  distribution by fitting the phase  $\phi$  predicted by the model to the measured phase  $\phi_{meas}$ . As an example, this fitting can be optimized in the least squares sense as

$$\sigma_{rec} = \operatorname{argmin} \|\phi(\sigma) - \phi_{meas}\|^2 \quad (8)$$

where  $\sigma_{rec}$  is the spatial distribution of the electrical conductivity reconstructed by fitting  $\phi(\sigma)$  to  $\phi_{meas}$ . This fitting is accomplished by adjusting  $\sigma$  to minimize the discrepancy between  $\phi(\sigma)$  and  $\phi_{meas}$  in the L2-norm sense; the dependence of the model predicted phase  $\phi$  on  $\sigma$  is explicitly shown in (8).

To account for noisy phase measurements, a regularization term [21] is adopted to stabilize the inversion, transforming (8) into

$$\sigma_{rec} = \operatorname{argmin} \left[ \|\phi(\sigma) - \phi_{meas}\|^2 + \alpha \Psi(\sigma) \right] \quad (9)$$

where  $\alpha$  is a scalar Tikhonov factor controlling the amount of regularization and  $\Psi(\sigma)$  is a regularization functional. These functionals are often quadratic and involve first or second differential operators [21], but many different forms beyond simple differential operators have been proposed in literature. Two different functionals often used in inverse problems, Quadratic Regularization and Total Variation Regularization, are described and implemented here.

### IV. IMPLEMENTATION

In order to implement an MR-EPT reconstruction based on (9), a regularization functional needs to be defined, a numeric method for computing  $\phi(\sigma)$  as defined by (5) and (7) must be implemented, and the Jacobian matrix of the mapping  $\sigma \mapsto \phi(\sigma)$  needs to be computed.

#### A. Quadratic Regularization

In a first implementation example, a classical quadratic functional can be used to transform (9) into

$$\sigma_{rec} = \operatorname{argmin} \left[ \|\phi(\sigma) - \phi_{meas}\|^2 + \alpha \|L\sigma\|^2 \right] \quad (10)$$

where  $\sigma$  is discretized on the same pixel grid as that used by the MR scanner to map  $\phi_{meas}$ . This converts  $\sigma$  from a continuous function into a finite vector of discretized values. The matrix  $L$  is a regularization matrix, which we have chosen to be the Laplacian of the conductivity distribution, a relatively common choice [22], [23].

By applying the Newton-Raphson method to (10), an update equation for the conductivity can be derived as

$$\begin{aligned} \delta\sigma = & -[J^T J + \alpha L^T L]^{-1} \\ & \times [J^T (\phi(\sigma) - \phi_{meas}) - \alpha L^T L(\sigma - \sigma^*)] \end{aligned} \quad (11)$$

where  $J$  is the Jacobian matrix of the mapping  $\sigma \mapsto \phi(\sigma)$ , and  $\sigma^*$  is an initial conductivity distribution. A uniform conductivity can be used as an initial starting distribution  $\sigma^*$  and updated using (11), as  $\sigma_{rec} = \sigma^* + \delta\sigma$ . A single update is sufficient in this case since the forward model is linear in  $\sigma$ . As a result, the Newton-Raphson method finds the solution to (10) in one step. In order to apply (11) one has to compute  $\phi(\sigma)$  and the Jacobian matrix  $J$ .

The forward problem  $\sigma \mapsto \phi(\sigma)$  in three dimensions consists of solving

$$\frac{\partial^2 \phi}{\partial x^2} + \frac{\partial^2 \phi}{\partial y^2} + \frac{\partial^2 \phi}{\partial z^2} = \mu\omega\sigma \quad (12)$$

where the  $(x, y, z)$  are the coordinates in the axes  $(\vec{x}, \vec{y}, \vec{z})$ , which are defined to be aligned to the main axes of the image stack. The Partial Differential (12) can be easily discretized on the image grid using Finite Difference schemes [24] expressing the partial derivatives as

$$\frac{\partial^2 \phi}{\partial x^2} = \frac{\phi(x+h_x) - 2\phi(x) + \phi(x-h_x)}{h_x^2} \quad (13a)$$

$$\frac{\partial^2 \phi}{\partial y^2} = \frac{\phi(y+h_y) - 2\phi(y) + \phi(y-h_y)}{h_y^2} \quad (13b)$$

$$\frac{\partial^2 \phi}{\partial z^2} = \frac{\phi(z+h_z) - 2\phi(z) + \phi(z-h_z)}{h_z^2} \quad (13c)$$

where  $h_x, h_y, h_z$  are respectively the pixel spacings along the  $x, y, z$  axes and the points  $(x - h_x), x, (x + h_x), (y - h_y), y, (y + h_y), (z - h_z), z$ , and  $(z + h_z)$  translate into the indices within the vector of discrete phases  $\phi$ . As is standard in Finite Differences, the partial differential equation (12) can be transformed into a linear system

$$A\phi = b \quad (14)$$

where  $A$  is a matrix derived from applying (13) to the different pixels in the image,  $b$  is a right hand side (RHS) derived from the evaluation of the term  $\mu\omega\sigma$  in (12) at each pixel location in the image, and  $\phi$  is the vector of computed phase values.

Appropriate boundary conditions need to be applied to the linear system in (14). The following approach is used here

- **Boundary Pixels:** Dirichlet boundary conditions are established for all the pixels on the boundary surface of the image stack by placing a 1 on the diagonal element  $A(i, i)$ , where  $i$  is the index of each of these pixels, and setting  $b(i) = \phi(i)_{meas}$ .
- **Internal Pixels:** for all the pixels internal to the domain (defined as being at least 1 pixel away from the boundary), (13) is applied and the RHS is computed as  $b(i) = \mu\omega\sigma(i)$ , where  $i$  is the index of the considered pixel.

Solving the linear system (14) results in the vector  $\phi$  of computed phase values.

A similar approach is used for building the matrix  $L$ , which is a Laplacian operator. The purpose of  $L$  is to limit high frequency spatial variations in the image, which typically arise from noise in the data. The term  $\|L\sigma\|^2$  takes large values for large spatial variations or for high frequency spatial variations in  $\sigma$ , which penalizes their presence in the reconstructed image (10). Elements of  $L$  corresponding to the interior domain are computed using the same finite differences applied to solve the forward problem (13). Elements of  $L$  corresponding to the domain boundary are defined using mirroring boundary conditions. Specifically, if the term  $(x + h_x)$  in (13a) falls outside the domain,  $(x + h_x)$  is assumed equal to  $(x - h_x)$  and the second derivative for that image location is expressed as:

$$\frac{\partial^2 \phi}{\partial x^2} = \frac{-2\phi(x) + 2\phi(x - h_x)}{h_x^2}. \quad (15)$$

Similar conditions are used for derivatives in  $y$  and  $z$ .

The Jacobian matrix in (11) can be computed from (14) using the following matrix identities

$$J = \frac{\partial \phi}{\partial \sigma} = \frac{\partial (A^{-1}b)}{\partial \sigma} = A^{-1} \frac{\partial b}{\partial \sigma} = A^{-1} \xi \quad (16)$$

where  $\xi$  is the derivative of  $b$  with respect to  $\sigma$ . In this case,  $\xi(i) = 0$  for all indices  $i$  corresponding to boundary pixels (for which the Dirichlet condition has been set) and  $\xi(i) = \mu\omega$  for all the indices corresponding to interior pixels where  $b(i)$  is set to  $b(i) = \mu\omega\sigma(i)$ . Equations (14) and (16) enable calculation of  $\phi$  and  $J$ , which are in turn used in (11) to compute  $\sigma_{rec}$ .

As shown later, the above procedure results in successful reconstructions on synthetic and experimental data. The use of the quadratic regularization functional produces conductivity profiles that are relatively smooth. The benefit of the inverse formulation developed here (9) is that different functional terms can

be used for regularization. In the next subsection, Total Variation is introduced as an alternative regularization term.

### B. Total Variation Regularization

In the previous sections, a framework for MR-EPT image reconstruction based on inverse problems was developed. One benefit of this framework is that different regularization terms can be chosen. Regularization functionals affect how the reconstructed image is smoothed and different choices are appropriate for different situations. Total Variation (TV) is a relatively novel form of regularization that results in images with sharper conductivity transitions as compared to Quadratic Regularization approaches (e.g. 11). Reconstructing sharp image transitions can be challenging in MR-EPT. In direct approaches derivatives are estimated on multiple points (e.g. 5, 7, or 9) to reduce noise sensitivity, but this results in smoothing. In the inverse approach described above the regularization smooths the reconstructed image, again for reducing sensitivity to noise. The use of TV regularization instead allows reconstructing fast spatial variations more accurately.

The TV-based inverse formulation for (9) is expressed as

$$\sigma_{rec} = \operatorname{argmin} \left[ \|\phi(\sigma) - \phi_{meas}\|^2 + \alpha TV(\sigma) \right] \quad (17)$$

where the TV functional is defined as  $TV(\sigma) = \int_{\Omega} |\nabla(\sigma)| d\Omega$  and  $\Omega$  is the imaging domain. The sharper reconstructions possible with TV regularization arise because the TV functional remains finite for step changes, while quadratic functionals like  $\int_{\Omega} |\nabla(\sigma)|^2 d\Omega$ , or,  $\int_{\Omega} |\nabla^2(\sigma)|^2 d\Omega$  (common quadratic regularization functionals) tend towards infinity. As a result of the large quadratic functional values associated with fast spatial changes in conductivity, these profiles (i.e. step changes in conductivity) are penalized, rendering the reconstructions smoother. More detailed discussion of the TV function properties are presented in [12].

While the use of TV is desirable for reconstructing sharp variations, the image reconstruction expressed by (17) is a non-differentiable optimization problem, and special techniques need to be employed to minimize  $\|\phi(\sigma) - \phi_{meas}\|^2 + \alpha TV(\sigma)$  when acting on  $\sigma$ . In this case, a Primal Dual-Interior Point framework developed in [25], [26] for optimizing (17) was used. Specifically, the algorithm named “PD-IPM-L2-L1 Norm” reported in [25] is used. The MR-EPT forward model  $\phi(\sigma)$  and Jacobian matrix  $J$  developed in Section IV-A are input into the optimization algorithm, resulting in  $\sigma_{rec}$  as defined in (17).

In Sections V and VII, numerical and experimental data are used respectively to compare these two regularization approaches and demonstrate how the smoothing/sharpening characteristics of the reconstruction can be tuned by the regularization functional.

## V. NUMERICAL EXPERIMENTS

A number of numerical experiments were conducted to validate this inverse formulation for MR-EPT conductivity reconstruction. The simulated volume of interest consists of a cubic block of  $20 \times 20 \times 20$  millimeters split in half by passing a plane through the center of the cube. One half of the cube is set to have a conductivity of  $1 \text{ Sm}^{-1}$  while the other half is set to

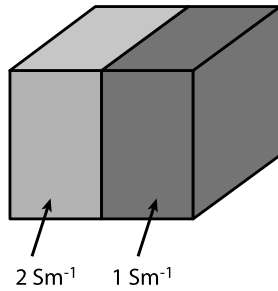


Fig. 1. Simulated domain used for the numerical experiment: a  $20 \times 20 \times 20$  mm cube with a conductivity of  $1 \text{ Sm}^{-1}$  on one side and of  $2 \text{ Sm}^{-1}$  on the other was generated in MATLAB. The simulation of the MR phase within the cube was computed for a 3 T magnet using a Finite Difference discretization with 1 mm resolution, using the modeling approach developed in Section II.

$2 \text{ Sm}^{-1}$ , as shown in Fig. 1. While these simulated conductivities are generally larger than typical physiological values, they serve as a good test to demonstrate that the algorithms can reconstruct a unit step change from 1 to  $2 \text{ Sm}^{-1}$  at the interface between the two halves of the numerical phantom.

The simulated cube was discretized into  $1 \times 1 \times 1$  mm volume elements, and Finite Differences were used to compute the MRI phase using equations (12) to (14), and assuming a 3 Tesla static magnet strength. A Dirichlet boundary condition of  $\phi(r) = 0 \quad \forall r \in \partial\Omega$  was assumed on the boundary. As discussed in Section II, Dirichlet boundary conditions can be used for matching a measured phase at the domain boundary while computing the forward solution. In the absence of boundary data, the condition  $\phi(r) = 0 \quad \forall r \in \partial\Omega$  is a practical condition that is compatible with the Poisson equation and results in a unique solution. This choice does not alter the reconstructed conductivity, which depends on the Laplacian of the phase—the value of which is enforced within the domain by the Poisson equation itself.

Fig. 2(a) shows a 2D cross section of the computed synthetic phase; Fig. 2(b) shows the same synthetic phase with 20% additive Gaussian noise, as discussed later and as used in the reconstructions. The curvature (i.e. Laplacian) of the phase is more pronounced in the left part of the domain due to the higher conductivity ( $2 \text{ Sm}^{-1}$ ) within this region.

The simulated phase data was input into three different reconstruction algorithms. The first is an implementation of the direct approach developed by Katscher *et al.* [3]. This algorithm is based on numerically solving (2) and using a volume of integration to improve robustness to noise. Specifically, the order of differentiation is decreased from 2nd to 1st order using the Gauss theorem to convert the volume integral of (2) to a surface integral which has only first derivatives of the field variables. This represents an approach that directly computes the output conductivity as a function of the input phase distribution by taking 1st order derivatives and computing their integral over specific integration volumes. In our implementation of this algorithm, an integration volume of  $5 \times 5 \times 5$  pixels was defined and phase derivatives were estimated using Savitzky-Golay [27] filters involving 7 points (three points per side of the considered pixel). Katscher *et al.* uses similar integration volumes, and 5 to 9 points for derivative estimation. We found that, for our numerical data, using only 7 points represents a good compromise be-

tween image sharpness and noise sensitivity, while larger numbers of points lead to smoother images with limited ability to identify sharp transitions. The second and third algorithms are implementations of the inverse formulation approach developed in this manuscript with Quadratic Regularization (10) and with TV regularization (17), respectively.

Reconstructions for the three different algorithms are shown in Fig. 3 using a fixed gray-scale for all figures spanning conductivity values from 0.5 to  $2 \text{ Sm}^{-1}$ . The top row of the figure represents reconstruction with our own implementation of the algorithm proposed in [3], the second row represents reconstruction with the inverse algorithm using Quadratic Regularization, and the last row reconstructions with the inverse algorithm using TV regularization. Different levels of simulated noise were added to the phase data for each column of the reconstructions. Specifically, noise levels of 5%, 10%, 15%, and 20% were added to columns 1 to 4, respectively. Noise was generated by extracting values from a Gaussian random distribution. These values were scaled to generate a particular percent noise level (5% to 20%) and added to the noiseless simulated phase of Fig. 2. As an example, for a 1% noise level, an input noise image  $\nu$  is scaled such that  $(\text{std}(\nu)/\text{std}(\phi)) = 0.01$ , where  $\text{std}$  indicates the standard deviation. Fig. 2(b) shows an example 2D cross section of the noisy simulated phase for a 20% noise level.

For the two inverse algorithms an optimal value of the Tikhonov factor was found empirically, and used for each of the different noise levels. A value of  $1 \times 10^{-5}$  was used for the Quadratic Regularization reconstruction, and a value of  $5 \times 10^{-6}$  for the TV reconstruction. The effect of the choice of the Tikhonov value is discussed later in this Section.

The direct algorithm successfully reconstructs the phase information, showing a higher conductivity on the left side of the domain, and a vertical transition between the more conductive and less conductive regions. The gray, 3-pixel wide, band present at the boundary of the image is an artifact of using derivative filters, which cannot operate in proximity of the boundary; the derivative filters used here require three pixels per side of the considered pixel. The inverse quadratic algorithm successfully reconstructs the conductivity profile showing a more conductive and a less conductive region on the left and right sides, respectively. This algorithm provides a similarly smooth transition at the conductivity boundary as compared to the direct algorithm, but visually is more stable in the presence of noise. Total Variation-based reconstructions exhibit a sharp transition in the conductivity distribution, resulting in a better overall estimation of the original data. This algorithm is also the least sensitive to noise for this dataset. TV is an appropriate image prior for distributions with sharp transitions like the one used for these tests, and therefore likely to produce better results compared to other methods. All the images produced by the inverse approach present a border of one pixel. Pixels on the boundary are not estimated as they can be affected by the boundary condition  $\phi(r) = \phi(r)_{\text{meas}}$ .

Fig. 4 shows the effect of the Tikhonov factor on the reconstructed images. This figure shows 2D cross-sections of three-dimensional reconstructions with the Quadratic Regularization inverse algorithm for a noise level of 10% and for different values of the Tikhonov factor, which are, from

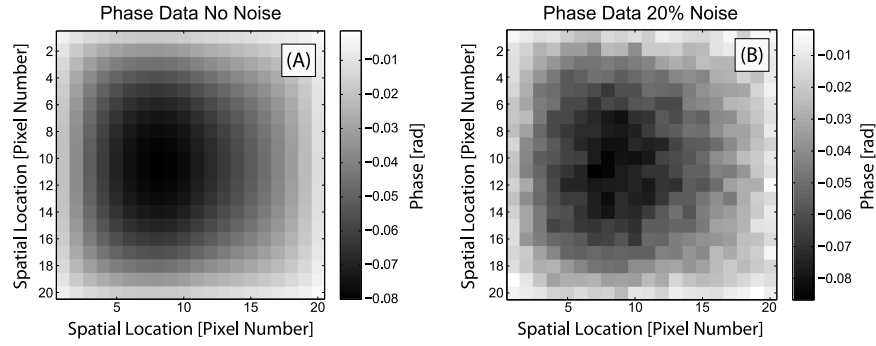


Fig. 2. 2D cross section in the horizontal plane of the 3D computed MRI phase for the conductivity distribution shown in Fig. 1. Subfigure (A) shows the noiseless phase, and subfigure (B) the noisiest phase (20% noise level) fed into the numerical simulations. As expected the computed phase has a higher curvature corresponding to the more conductive region (left of the picture), as the Laplacian takes larger values for high conductivity regions compared to less conducting regions (right of the picture). The units used for plotting the phase are radians, and the range is -0.08 to 0.00 radians.

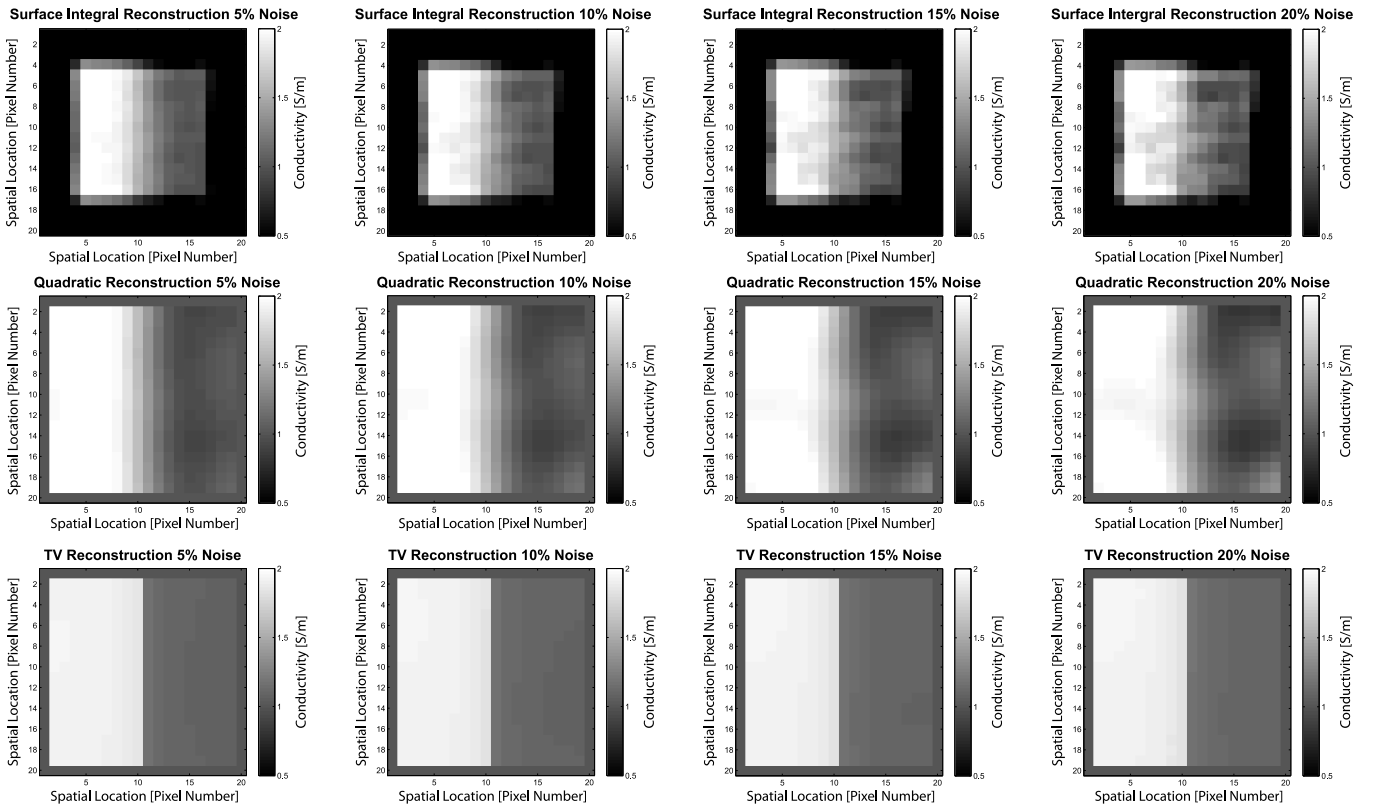


Fig. 3. 2D cross-sections of three-dimensional reconstructions of synthetic phase data with noise levels of 5%, 10%, 15%, and 20%, associated with columns 1 to 4, respectively. Each row in the figure represents a reconstruction with a different algorithm: the top row shows (for different levels of noise) reconstructions with our own implementation of the algorithm proposed in [3]. We use an integration volume of  $5 \times 5 \times 5$  pixels, and estimate derivatives on 3 pixels per side of the central pixel, this results in a band, 3-pixels wide, around the image that cannot be reconstructed. The reconstruction successfully identifies the conductivity distribution, showing a left-to-right transition. The second and third row of the figure represent reconstructions with the developed inverse approach, using Quadratic Regularization (QR) and Total Variation (TV) regularization, respectively. The QR algorithm is able to identify the left-to-right change in conductivity and to describe it with a certain degree of smoothness, which is characteristic of this type of regularization. The TV algorithm is able to identify and describe with pronounced sharpness the left-to-right change in conductivity. In this specific case the TV algorithm also appears particularly robust to noise. For both QR and TV algorithms an optimal Tikhonov factor was found empirically, and maintained constant across the different levels of noise. Specifically a value of  $1 \times 10^{-5}$  and of  $5 \times 10^{-6}$  was used respectively for the two algorithms. With the parameters used, the inverse based algorithms seem to fare better in the presence of noise compared to the direct algorithm, as it would be expected from the fact that they do not need to differentiate input phase data. All figure are represented on a grayscale ranging from 0 to  $2 \text{ Sm}^{-1}$ .

left to right,  $1 \times 10^{-7}$ ,  $1 \times 10^{-6}$ ,  $1 \times 10^{-4}$ , and  $1 \times 10^{-3}$ . These values bracket the optimal value of  $1 \times 10^{-5}$  used in the reconstructions of Fig. 3. The two left reconstructions are under-regularized (i.e. a too small Tikhonov value results in noisy images). The two right reconstructions are instead over-regularized (i.e. a too large value of Tikhonov factor

results in reconstructions that are not as sensitive to noise, but in which the spatial transitions have been smoothed excessively). The value of  $1 \times 10^{-5}$  used in Fig. 4 therefore represents a good compromise between sensitivity to noise and resolution.

Conductivity profiles across the middle of the domain and passing through the transition point were extracted from the

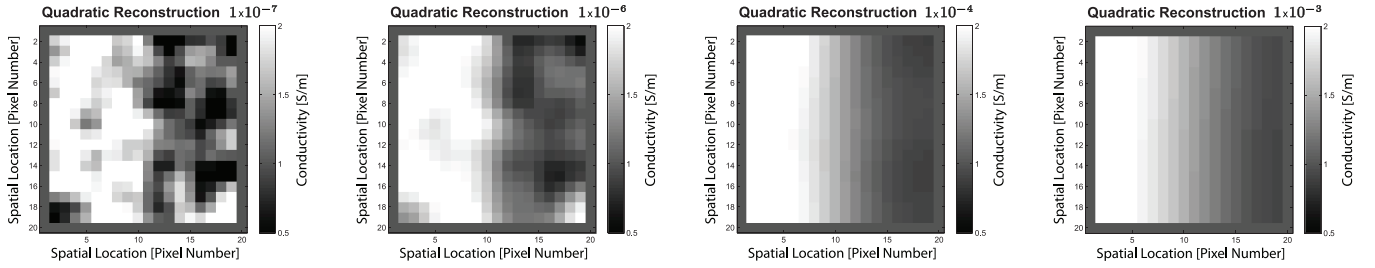


Fig. 4. Effect of the Tikhonov factor on reconstruction. The four figures show 2D cross-sections of three-dimensional reconstructions of synthetic phase data with a fixed noise level of 10% and a varying Tikhonov factor of a value of  $1 \times 10^{-7}$ ,  $1 \times 10^{-6}$ ,  $1 \times 10^{-4}$ , and  $1 \times 10^{-3}$ , from left to right. The chosen values bracket the optimal value of  $1 \times 10^{-5}$ , which was found empirically and used in the reconstructions in Fig. 3. The values  $1 \times 10^{-7}$  and  $1 \times 10^{-6}$  result in an under-regularized image which is sensitive to noise. The values of  $1 \times 10^{-4}$ ,  $1 \times 10^{-3}$  result in images that are over-regularized, where sensitivity to noise has been greatly reduced, but spatial transitions have been overly smoothed. All figures are represented on a grayscale ranging from 0 to  $2 \text{ Sm}^{-1}$ .

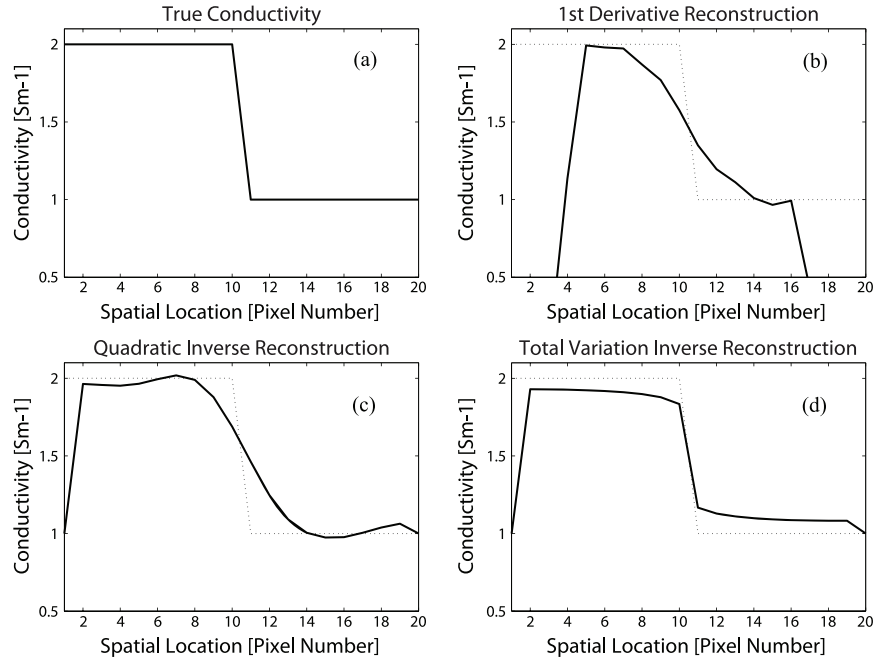


Fig. 5. Subfigure A shows a plot of the conductivity value on a horizontal line crossing the cube of Fig. 1, where the vertical axis represents the conductivity value and the horizontal axis the position along the left-to-right direction inside the conductivity cube. Subfigures B, C, and D represent a similar plot for the reconstructed conductivity values, for a noise level of 10%, respectively for our own implementation of the algorithm proposed in [3], for the inverse reconstruction with Quadratic Regularization, and for the inverse reconstruction with Total Variation regularization. In these three subfigures the bold continuous line represents the reconstructed values, and the thin dotted line the true conductivity value, as in subfigure A. The algorithm in subfigure B and C have a similar performance in terms of how steeply they can describe the sharp transition, while the algorithm in subfigure D (Total Variation) is able to describe the step conductivity change much more accurately.

three reconstructions with the three different algorithms for the 10% noise level case, and are shown in Fig. 5. The original conductivity profile (Fig. 5(a)) used for generating the synthetic phase data shows the true transition each algorithm attempts to recover. The bold lines depict the reconstructed profile, while the true conductivity profile is shown as a dotted line in Figs. 5(a), 5(b), and 5(c). While the direct approach (Fig. 5(a)) and the inverse approach with Quadratic Regularization (Fig. 5(b)) are substantially equivalent in terms of how fast they describe the transition from high conductivity to low conductivity, the reconstruction with TV regularization (Fig. 5(c)) shows a much steeper transition in the reconstructed profile, and is therefore a more accurate reconstruction of the step conductivity profile. The inverse formulation developed here enables one to select regularization functionals that are appropriate for the problem at hand. Besides TV and similar

edge-preserving techniques it is possible to envision using *ad-hoc* functionals that incorporate prior structural information extracted from other anatomic MR images [18], [19].

## VI. COMPUTATIONAL BURDEN CONSIDERATIONS

While the developed approach offers flexibility in terms of the regularization functionals available and does not require differentiating the noisy input images, it does require a higher computational load compared to methods based on direct differentiation. This computational burden can be measured in terms of number of computations and amount of working memory required. We will show that the computational burden can be significant, for images with a moderate number of pixels, but that it is possible to reduce it by subdividing the image domain and by reconstructing smaller subdomains individually. We will use

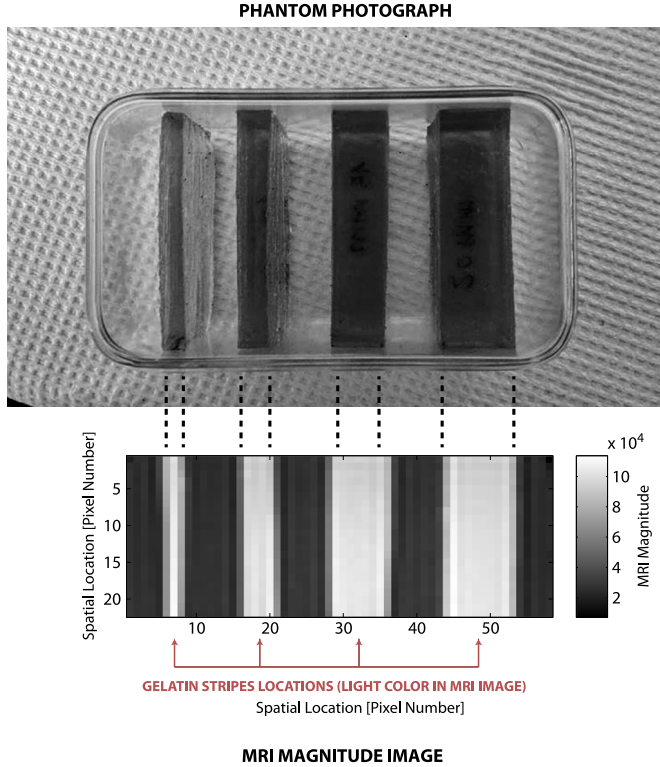


Fig. 6. Top: photographic representation of the conductivity phantom. A conductivity phantom was generated by slicing a slab of gelatin in slices of 20 mm, 15 mm, 10 mm, and 5 mm of thickness. The slices were positioned inside a polymer housing and secured to it by slightly heating the housing and letting the gelatin in contact with the housing walls slightly melt before re-solidification. The phantom was then filled with a saline solution (not shown). The gelatin had a conductivity of  $1.8 \text{ Sm}^{-1}$  and the saline solution of  $4.1 \text{ Sm}^{-1}$ . Copper sulfate ( $\text{CuSO}_4$ ) was added to the gelatin, so that the gelatin slabs would show with a different intensity in traditional MR amplitude images. Bottom: an MR amplitude image shows the phantom. Gelatin slices appear in a brighter gray due to the inclusion of Copper Sulfate (note that gelatin slices have a lower conductivity value compared to the saline solution ( $1.8 \text{ Sm}^{-1}$  versus  $4.1 \text{ Sm}^{-1}$ ), and therefore they appear darker in the MR-EPT reconstructions of Fig. 7).

this approach for reconstructing the experimental MRI data presented in Section VII.

Image reconstruction with the developed inverse formulation requires solving the forward problem (5), using for example a finite-difference scheme, and updating the conductivity or permittivity values with a Gauss Newton update as in (11). For moderate to relatively large imaging volumes solving (5) or (11) presents challenges. For example, an imaging volume of  $256 \times 256 \times 256$  pixels requires the forward problem to be solved for  $256^3$ , or more than 16 million unknowns. Problems of this size can be efficiently solved on a desktop computer in a few minutes of computation time using specialized algorithms, such as those based on Algebraic Multigrid Methods [28]. These algorithms are not readily available in computing environments like MATLAB, and require the user to procure specialized libraries. In addition to the time required for forward solving, there is a particular challenge posed by the memory utilization required to solve (11). The number of rows and columns in the Jacobian matrix  $J$  is equal to the number of unknowns in the problem. In the particular case of a  $256 \times 256 \times 256$  imaging domain, the Jacobian would be a  $256^3 \times 256^3$  matrix, requiring

memory allocation beyond the limits of any personal computer. The approach we have implemented subdivides the imaging domain into several smaller subdomains over which the Jacobian is formed; this significantly reduces the computational burden and memory requirements. For a  $N \times N \times N$  imaging domain, the size of the forward problem is  $N^3$  and the memory required for storing the Jacobian is proportional to  $N^3 \times N^3 = N^6$ ; dividing the domain into a small number of subdomains immediately reduces the computational burden.

If the domain is subdivided, for example into cubic blocks smaller than the full domain, the boundary condition (7) can be applied at the interface between the different blocks. The forward problem can then be solved (5) within each subdomain. Since (7) can be applied everywhere using the measured phase values, the forward problem can be solved on a subdomain independently from the neighboring subdomains, and image reconstruction carried out on each subdomain independently from others.

The only potential dependence between neighboring pixels is introduced at the interface between two imaging subdomains if the regularization matrix  $L$  in (11), or in the equivalent Total Variation formulation (17), correlates neighbouring pixels across the two different subdomains. In our current implementation, we do not regularize pixels across different imaging subdomains; this enables us to run fully independent reconstructions on portions of the full domain. For real MRI data (see Section VII), we split the imaging domain using this sub-domain technique to reduce the computational burden associated with the large number of pixels within the MR image stack. The number of pixels recorded during a standard MR-EPT scan are significantly more than those used in our numerical simulation (Section V).

To substantiate the above discussion, we report the computational time and the required amount of memory for storing the Jacobian matrix for different subdomain sizes used for reconstructing the phantom in Fig. 9. The original MRI image (acquisition details described in Section VII) has a size of  $144 \times 144 \times 144$  pixels. Within this volume a region of interest (ROI) of  $61 \times 55 \times 5$  pixels was chosen to capture the curved detail of the phantom and to exclude the boundaries of the plastic container used to house it. A magnitude image of the selected ROI is shown in Fig. 9(b). The slices of the ROI were split in 1, 2, or 3 parts along the vertical and horizontal directions, giving rise to a number of smaller subdomains for image reconstruction. Precisely we used the following configurations:  $2 \times 1$ ,  $2 \times 3$ ,  $3 \times 2$ , and  $3 \times 3$ , where the first number indicates how many subdivisions were used along the vertical direction and the second number indicates the number of subdivisions along the horizontal direction. For example, the configuration  $3 \times 3$  results in 9 subdomains in total, where slices are subdivided with a 3 by 3 grid (see Fig. 10. All the information (5 slices) was used in the third dimension.

Table I reports timing and memory usage information. All computations were performed on a workstation with an Intel Xeon 3503 CPU running at 2.40GHz, with 8 GB of memory, using the Windows 7 Ultimate—64 bit operating system; algorithms were implemented and run in the MATLAB environment. An important difference exist between the algorithm

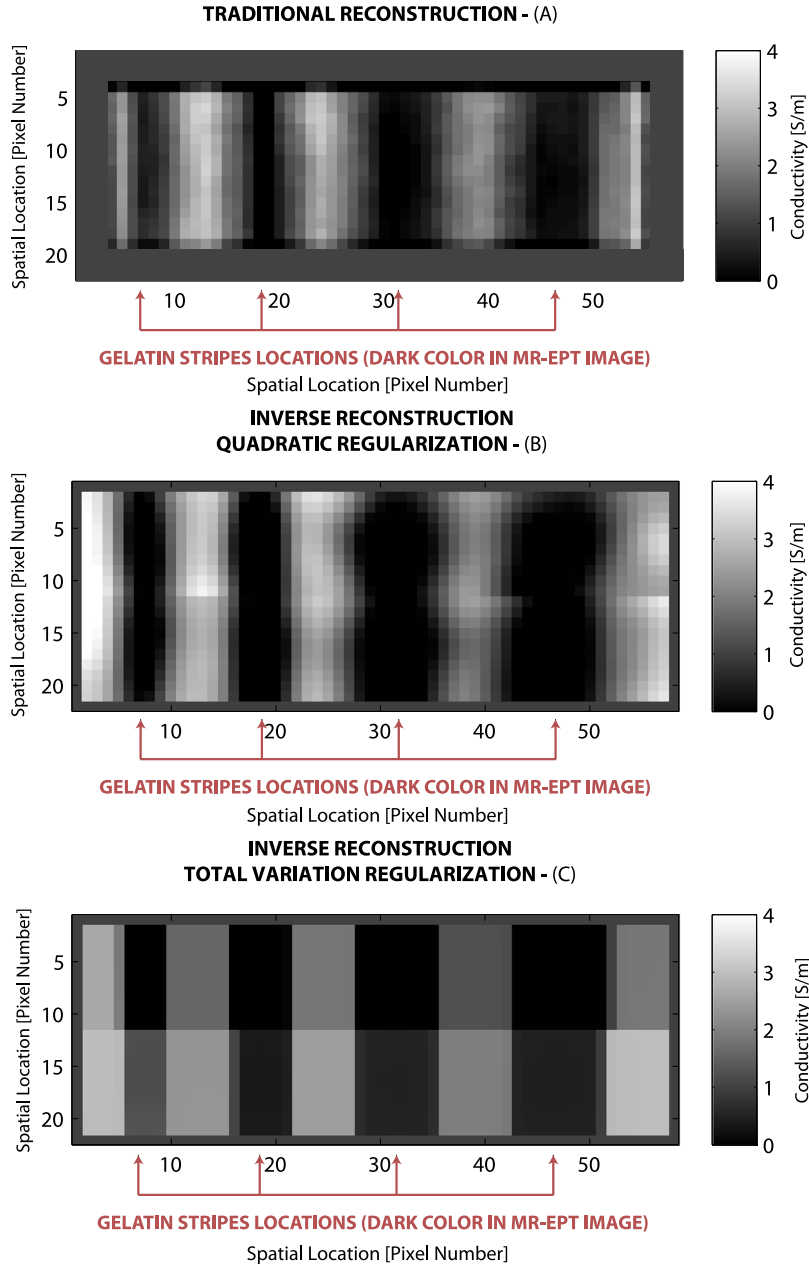


Fig. 7. MR-EPT Reconstructions of MR data acquired on the phantom of Fig. 6. Subfigure A shows a “traditional” MR-EPT reconstruction with our implementation of the algorithm proposed in [3]. A border of 3 pixels is present all around the boundary of the image, as derivatives are estimated using three pixel values per each side of the current pixel, therefore reconstruction can occur only for pixels that are at a distance of 3 pixels from the domain boundary. The algorithm reconstructs correctly the alternating conductivity values, corresponding to the high conducting saline solution, and less conducting gelatin slices. Gelatin slices appear in fact darker, as opposed to the lighter gray in which they appear in the MR magnitude image in Fig. 6(b), as the contrast mechanism in MR-EPT is based on the electrical properties, while the MR amplitude image is sensitive to the presence of Copper Sulfate. Subfigure B shows a MR-EPT reconstruction using the developed inverse formulation with Quadratic Regularization, and Subfigure C a MR-EPT reconstruction using the developed inverse formulation with Total Variation regularization. All figure are represented on a grayscale ranging from 0 to 4  $\text{Sm}^{-1}$ .

implementing Quadratic Regularization and the algorithm implementing Total Variation regularization (TV): the quadratic update equation (11) is linear with respect to  $\sigma$  (the Jacobian does not depend on  $\sigma$ ), and therefore the term  $[J^T J + \alpha L^T L]^{-1}$  only needs to be computed once, and can be applied later to any subdomain of the image—a fast matrix—vector multiplication. The Total Variation regularization algorithm instead requires an iterative cycle on each subdomain of the image (we use a fixed number of iterations, 10 cycles per subdomain), resulting in longer reconstruction times compared to

Quadratic Regularization (QR). For both algorithms computing was performed in double precision, timing and memory usage information is therefore relative to an 8-byte representation of floating point values. The coarser subdivision,  $2 \times 1$ , requires 61 seconds to compute with QR and 685 seconds with TV, using 162 Megabytes. These timing and memory requirements reduce respectively to 1.5 and 86 seconds for the smaller  $3 \times 3$  subdomain configuration, and to 7 MB of memory for Jacobian storage. While the QR algorithm, for smaller subdomains, presents a computational burden that is not dissimilar to that

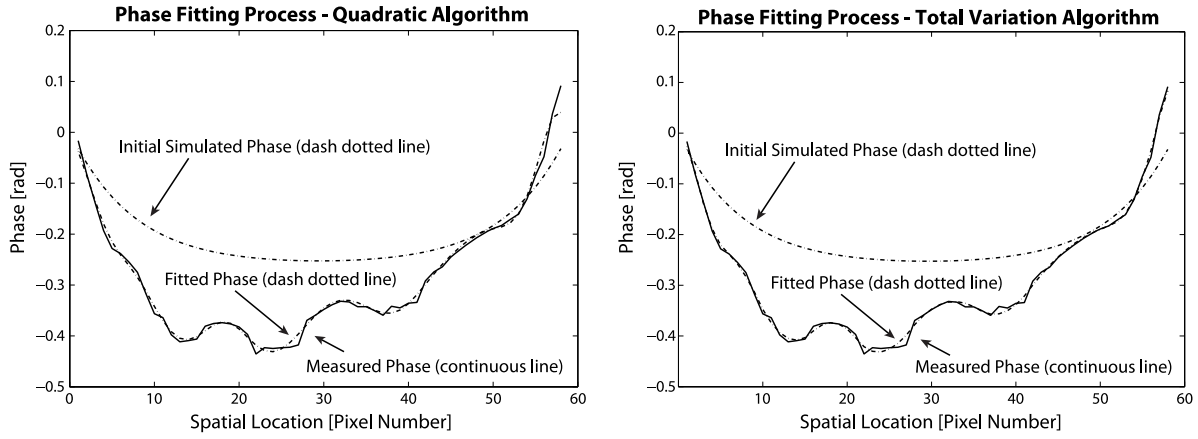


Fig. 8. Phase fitting process. This figure shows how the MR-EPT inverse reconstruction algorithm is fitting the phase data. The plot on the left shows results relative to the QR algorithm, and the plot on the right result relative to the TV algorithm. The dash-dotted line at the top of the plots represents the computed phase value across a numerical phantom of Fig. 6 corresponding to a uniform initial distribution of conductivity. The solid bold line at the bottom of the plots represents the true measured phase across the phantom. The dips and peaks of the measured phase represent phase changes corresponding to the alternating high-low conductivity values encountered across the gelatin stripes and saline volumes that constitute the phantom (see Fig. 6(a)). The dash-dotted line at the bottom of the plots represents the fitted phase, resulting from the inversion procedure. Despite reconstructed images looking quite different for the QR and TV algorithms, the fitted phases show minor differences. This is to be expected, as different values of reconstructed conductivity can stem from minor curvature changes in the phase. For both algorithms the fitted phase follows closely the general trends of the measured phase; regularization techniques used in the algorithm help to ensure that the model does not “overfit” the small scale phase perturbations that represent noise in the data (e.g. small dip near pixel position 20).

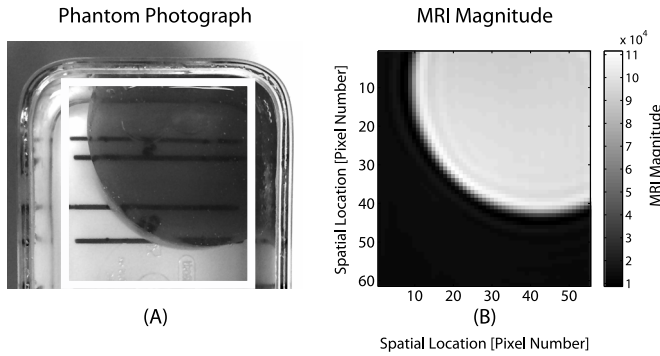


Fig. 9. Curved phantom photographic image (left) and MRI magnitude image (right). This phantom was built with a similar method to the phantom shown in Fig. 6, by creating a gelatin slab which is immersed in a saline solution. The gelatin slab has a conductivity of  $1.8 \text{ Sm}^{-1}$  and Copper sulfate ( $\text{CuSO}_4$ ) was added to it, to generate contrast in the MRI magnitude image. The saline solution has a conductivity of  $4.1 \text{ Sm}^{-1}$ . In part (A) of the figure is indicated a white edge that approximates the perimeter of a region of interest which was selected for image reconstruction. Part (B) of the figure shows the MRI magnitude corresponding to the region of interest used in the reconstructions of Fig. 7.

of direct approaches, TV reconstruction, as implemented in our algorithm, still presents a burden that is significant. Use of TV regularized reconstruction is therefore a tradeoff between the benefits offered by this type of functional and the time consumed in the reconstruction.

## VII. PHYSICAL EXPERIMENTS

The proposed MR-EPT reconstruction approach is demonstrated on two phantom datasets acquired using a Philips Achieva 3 T MR scanner using a Philips SENSE Flex S transmit/receive coil. A first conductivity phantom was prepared by slicing a  $12 \text{ cm} \times 7 \text{ cm} \times 5 \text{ cm}$  block of gelatin ( $\sigma = 1.8 \text{ Sm}^{-1}$ ) into slabs of different thicknesses (see Fig. 6). Specifically, slice thickness of 20 mm, 15 mm, 10 mm, and 5 mm were formed and placed into a polymer housing. The slices

TABLE I  
COMPUTATIONAL TIME FOR DIFFERENT SUBDOMAIN CONFIGURATIONS

Config.	Time QR Recon [s]	Time TV Recon [s]	Jac. Mem. [MB]
2x1	50.9	684.8	162
2x2	8.8	232.9	39
3x2	3.5	133.3	16
3x3	1.5	85.9	7

were positioned inside the housing and adhered to the walls by slightly heating the container; the heating causes a thin layer of gelatin to melt and re-solidify providing adhesion. Gelatin was prepared by using 10% by weight of dry porcine gelatin, and approximately 1% by weight of NaCl to adjust conductivity to the desired level. A saline solution with a conductivity of  $4.1 \text{ Sm}^{-1}$  was produced using approximately 2% NaCl in weight and used to fill the gaps between the slices of gelatin (not shown in Fig. 6), to provide an inclusion (gelatin) to background (saline) contrast. In addition, approximately 1% by weight of copper sulfate ( $\text{CuSO}_4$ ) was added to the gelatin, but not to the saline, in order to provide MR contrast.

Standard MR images (e.g. T1-weighted and T2-weighted) were not expected to detect the electrical properties contrast between the gelatin and the saline solutions; the  $\text{CuSO}_4$  provides MR contrast so that the structure of the phantom can be appreciated in standard MR images. MRI magnitude images depict a high intensity (white) where the gelatin slabs are located (corresponding to the high concentration of  $\text{CuSO}_4$ ), while the saline solution appears as a low intensity (black) region (see Fig. 6). This magnitude MR image provides a high resolution image of the experimental configuration to which reconstructed MR-EPT images can be compared. A standard Spin Echo (SE) MRI sequence was utilized for acquiring the magnitude and phase data, with the following settings: resolution of  $80 \times 80 \times 20$  pixels, field of view (FOV) of  $160 \times 160 \times 60 \text{ mm}$ , repetition time

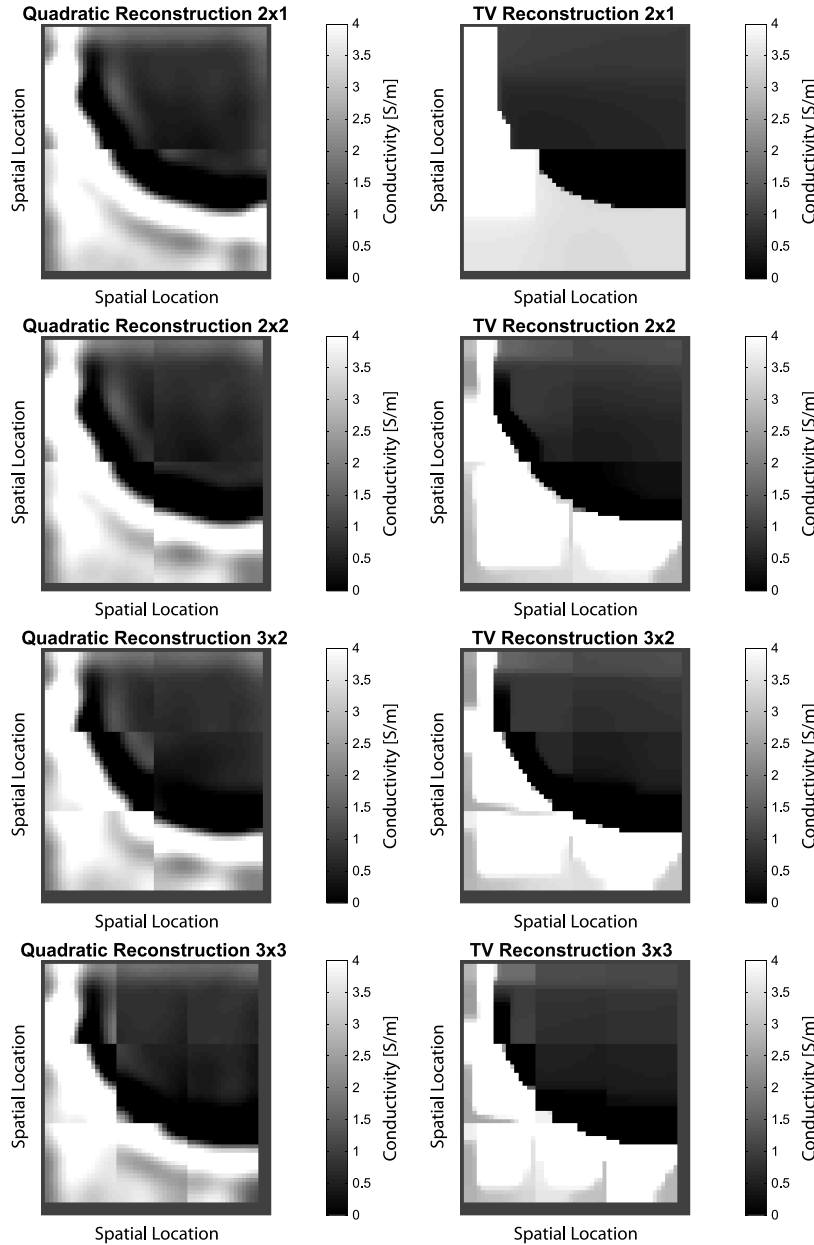


Fig. 10. 2D cross-sections of three-dimensional reconstructions of the phantom of Fig. 7. This figure demonstrates the ability of the inverse algorithms to reconstruct curved boundaries, and also serves to demonstrate the possibility of speeding up image reconstruction by splitting the image domain in smaller subdomains to be reconstructed independently. The left column represents reconstructions with the inverse algorithm with Quadratic Regularization and the right column reconstructions using Total Variation regularization. Each row represents a different subdomain splitting for image reconstruction, as discussed in Section VI. In the top row MRI slices have been split in two parts vertically, indicated as  $2 \times 1$  splitting, in the second row the slices have been split in two parts vertically and horizontally, indicated as  $2 \times 2$  splitting, and the third and fourth represent respectively  $3 \times 2$  and  $3 \times 3$  splittings. Splitting the original image domain in smaller parts allows for a faster reconstruction as discussed in Section VI and reported in Table I. Some discontinuities are present at those image locations where two different subdomains meet. This results from the fact that different subdomains are treated as separate by the reconstruction and no continuity is enforced. In future work we intend to introduce some correlation between neighbouring subdomains, through regularization techniques, which should reduce or eliminate these discontinuities. In both sets of reconstructed images, though some minor discontinuities are present at the interface between subdomains both and inverse QR and inverse TV algorithms are able to correctly reproduce the curved interface. All figures are represented on a grayscale ranging from 0 to  $4 \text{ Sm}^{-1}$ .

(TR) = 600 ms, and echo time (TE) = 7.79 ms. Four temporal averages were used in order to improve the SNR for a total acquisition time of 389 seconds. MR phase information was captured together with amplitude information and used for reconstructing conductivity images with the inverse implementation and with the direct method proposed by Katscher *et al.* [3]. For the inverse formulation, both Quadratic Regularization and TV-based regularization approaches were used. For all reconstructions, data extracted from a central portion of the phantom,

consisting of a  $58 \times 22 \times 7$  pixel volume, was used. All three reconstruction approaches exhibit regions of high and low conductivity corresponding to the saline and gelatin, respectively (see Fig. 7). The same grayscale was selected for each of the different algorithms, ranging from  $0 \text{ Sm}^{-1}$  (black) to  $4 \text{ Sm}^{-1}$  (white). It is important to note that gelatin slices present a lower conductivity ( $1.8 \text{ Sm}^{-1}$ ) compared to the saline solution ( $4.1 \text{ Sm}^{-1}$ ), making the gelatin slices appear in a darker gray level. This is in contrast to MR magnitude images (Fig. 6), where

gelatin slices appear brighter due to the presence of ( $\text{CuSO}_4$ ). These contrast differences observed between MR magnitude images (Fig. 6) and MR-EPT reconstructions (Fig. 7) help to validate MR-EPT's dependence on conductivity and not on typical MR contrast mechanisms (e.g.  $\text{CuSO}_4$ ).

All three reconstruction approaches correctly identify the location of the gelatin strips within the phantom (Fig. 7). The reconstruction using our implementation of the direct method developed by Katscher *et al.* [3] has a border of 3 pixels over which the conductivity values are not reconstructed. This artifact stems from using Savitzky-Golay filters with 3 pixels on each side of the central pixel of interest to estimate the derivatives at these locations. In the inverse formulation, a single pixel around the border is used to match the measured phase with the Dirichlet boundary condition (7) and is not reconstructed; all other interior pixels are fit to the data. In this particular experimental configuration, the reconstruction with Quadratic Regularization (Fig. 7(b)) provides slightly more contrast as compared to the reconstruction based on integration of first derivatives (Fig. 7(a)). Much more noticeable is the difference between the reconstruction based on Total Variation (TV) (Fig. 7(c)) regularization and the other two reconstruction approaches. TV represents a good prior for describing the sharp conductivity transitions that are present at the gelatin-saline interface; using this form of regularization significantly enhances the reconstructed images. The reconstructed conductivity (Fig. 7(c)) geometrically aligns with the phantom configuration (as viewed visually and in MR magnitude images) in that the high conductivity gelatin regions (dark stripes) correspond to high intensity MR magnitude regions (light stripes). The TV-based regularization accurately identifies the steep transitions that are characteristic of the phantom, while the direct and quadratic-based inverse formulation do not recover the steep transitions. Both quadratic and TV-regularized inverse approaches to reconstruction (Fig. 7(b) and (c)) exhibit a conductivity discontinuity through the center of the image. This discontinuity arises from having subdivided the reconstruction domain into an upper and lower subdomain for the purpose of speeding-up reconstruction as discussed in Section VI. In the current implementation of this approach the different subdomains in which an image can be divided are reconstructed in a completely independent manner (i.e. we do not introduce correlation between neighbouring pixels at the interface of the subdomains in the regularization matrices), and results in small discontinuities observed in the images. Using a scheme that incorporates subdomain overlap as presented in [29] will be explored in the future to reduce or eliminate this artifact.

The fitting process resulting from the inverse approach to reconstruction can be evaluated by observing how the fitted phase progresses from the initial guess to the final reconstructed phase (Fig. 8). In this case, the estimated phase (y-axis) is plotted as a function of distance (x-axis) along a trajectory passing horizontally through the striped phantom for both the QR and TV algorithms. The dips and peaks in the phase data are caused by the varying conductivity values across the phantom gelatin slabs and saline volumes. True measured phase is indicated with a solid line, and the dash—dotted line at the top of the plots

represents the computed phase for an initial uniform conductivity distribution of  $1 \text{ Sm}^{-1}$ , while the dash—dotted line at the bottom of the plots represents the computed phase after the fitting is complete. The computed phase closely tracks the measured phase, with the exception of small-scale features associated with noisy measurements. The regularization helps to enforce an accurate fit of the measured phase, but to avoid fitting small scale variations that are typically associated with measurement noise and errors.

A second conductivity phantom was prepared using the same method described above for the striped phantom of Fig. 6. In this case though a portion of a round slab of gelatin was cut and placed in a corner of a polymer housing as shown in Fig. 9. This second physical phantom was used to evaluate the inverse reconstruction algorithms on a curvilinear geometry. The striped phantom of Fig. 6 is well suited for reconstruction with TV regularization algorithms, as it presents straight step changes, aligned with one axis of the image, that can be accurately reconstructed by TV algorithms. The curved boundary of the phantom in Fig. 9 poses a challenge to TV based algorithms, as they are known to tend to reconstruct round boundaries with a staircase appearance. The reconstructions of Fig. 10 demonstrate that both the QR and TV algorithms are able to capture and reproduce the curved nature of the boundary between gelatin and water. Both algorithms exhibit some artifact at the interface between subdomains, since we have not enforced any contiguity between the reconstructed values from different subdomains. TV regularization seems in this case to suffer less from the staircase effect compared to application in other tomographic applications. For example in Electrical Impedance Tomography the staircase effect seems to be more pronounced [25]. We believe this might be due to the fact that in MR-EPT data is measured everywhere in the domain and not only at the boundary as in other techniques. This might help to drive the reconstruction towards more realistic results.

## VIII. CONCLUSIONS

A novel approach to MR-EPT image reconstruction based on an inverse formulation has been developed. The approach is based on the observation that the central equations of MR-EPT can be inverted and used to describe a forward model, which in turn can be used in an inverse, data fitting approach to MR-EPT reconstruction. This approach is valid for reconstruction of conductivity from measured phase information and for reconstruction of permittivity from measured  $H^+$  amplitude information, though in the present manuscript we develop and demonstrate this approach only for reconstruction of conductivity. A forward model for computing phase information from conductivity data is presented (Section II). In addition, an inverse approach based on Quadratic Regularization and Jacobian computation has been developed for solving the MR-EPT image reconstruction problem (Section IV-A). An inverse formulation using Total Variation as a functional for regularization has been developed (Section IV-B); this approach enables the reconstruction of sharper conductivity transitions within the imaging domain. Numerical experiments were conducted to validate the developed inversion approaches in the presence

of synthetic noisy data (Section V). A method for splitting the imaging domain into subdomains has been developed to reduce the computational burden arising from the proposed inverse approach (Section VI); this implementation requires less memory utilization and fewer computations leading to faster reconstructions. Subdividing the imaging domain into smaller subdomains results in significant performance/memory utilization gains, as both the memory and computation time are linked to the size of the Jacobian matrix (which grows with the 6th power of the size of the imaging domain). Successful reconstructions were obtained on laboratory data collected from a phantom experiment that included alternating regions of high and low conductivity, and from a phantom with a curved boundary (Section VII). Both the inverse approach using Quadratic Regularization and the approach using Total Variation regularization accurately identified the position of the gelatin slabs; TV regularization more accurately reconstructed the steep conductivity transitions present at the gelatin-saline interface of the phantoms imaged. Benefits of this reconstruction method include: 1) no differentiation is required on the input data, therefore decreasing sensitivity to noise compared to other methods described in the literature; 2) different regularization functionals can be implemented, depending on the expected distribution of the parameters to be reconstructed. This capability is particularly useful in the context of reconstructing biomedical data, in such cases custom regularization functionals can be constructed *ad-hoc* to incorporate prior anatomical information and ultimately enhance the quality and robustness of the reconstructed images.

## REFERENCES

- [1] E. Haacke, L. Petropoulos, E. Nilges, and D. Wu, "Extraction of conductivity and permittivity using magnetic resonance imaging," *Phys. Med. Biol.*, vol. 36, no. 6, p. 723, 1991.
- [2] S. Akoka, F. Franconi, F. Seguin, and A. Le Pape, "Radiofrequency map of an NMR coil by imaging," *Magn. Reson. Imag.*, vol. 11, no. 3, pp. 437–441, 1993.
- [3] U. Katscher and , "Determination of electric conductivity and local SAR via B1 mapping," *IEEE Trans. Med. Imag.*, vol. 28, no. 9, pp. 1365–1374, Sep. 2009.
- [4] H. Wen, "Noninvasive quantitative mapping of conductivity and dielectric distributions using RF wave propagation effects in high-field MRI," *Med. Imag.*, pp. 471–477, 2003.
- [5] T. Voigt, H. Homann, U. Katscher, and O. Doessel, "Patient-individual local SAR determination: In vivo measurements and numerical validation," *Magn. Reson. Med.*, vol. 68, no. 4, pp. 1117–1126, 2012.
- [6] T. Voigt, U. Katscher, and O. Doessel, "Quantitative conductivity and permittivity imaging of the human brain using electric properties tomography," *Magn. Reson. Med.*, vol. 66, no. 2, pp. 456–466, 2011.
- [7] J. K. Seo *et al.*, "Error analysis of nonconstant admittivity for MR-based electric property imaging," *IEEE Trans. Med. Imag.*, vol. 31, no. 2, pp. 430–437, Feb. 2012.
- [8] X. Zhang, S. Zhu, and B. He, "Imaging electric properties of biological tissues by RF field mapping in MRI," *IEEE Trans. Med. Imag.*, vol. 29, no. 2, pp. 474–481, Feb. 2010.
- [9] D. K. Sodickson *et al.*, "Generalized local Maxwell tomography for mapping of electrical property gradients and tensors," in *Proc. 21st Annu. Meet. ISMRM*, Salt Lake City, UT, 2013, p. 4175.
- [10] F. S. Hafalir, O. F. Oran, N. Gurler, and Y. Z. Ider, "Convection-Reaction equation based magnetic resonance electrical properties tomography (cr-MREPT)," *IEEE Trans. Med. Imag.*, vol. 33, no. 3, pp. 777–793, Mar. 2014.
- [11] E. Balidemaj *et al.*, "CSI-EPT: A contrast source inversion approach for improved MRI-based electric properties tomography," *IEEE Trans. Med. Imag.*, vol. 34, no. 9, pp. 1788–1796, Sep. 2015.
- [12] L. I. Rudin, S. Osher, and E. Fatemi, "Nonlinear total variation based noise removal algorithms," *Physica D*, vol. 60, pp. 259–268, 1992.
- [13] K. M. Ropella and D. C. Noll, "A regularized model-based approach to phase-based conductivity mapping," in *Proc. 23rd Annu. Meet. ISMRM*, Toronto, ON, Canada, 2015, p. 3295.
- [14] A. Borsic, I. Perreard, and R. J. Halter, "MR-EPT reconstruction using an inverse formulation," presented at the 15th Int. Conf. Biomed. Appl. Electr. Impedance Tomogr., Gananoque, Canada, 2014.
- [15] A. Borsic, I. Perreard, and R. J. Halter, "An inverse approach to MR-EPT reconstruction," in *Proc. 22nd Annu. Meet. ISMRM*, Milan, Italy, 2014, p. 3191.
- [16] U. Katscher *et al.*, "Estimation of breast tumor conductivity using parabolic phase fitting," in *Proc. 20th Annu. Meet. ISMRM*, Melbourne, Australia, 2012, p. 2335.
- [17] J. Shin *et al.*, "Initial study on *in vivo* conductivity mapping of breast cancer using MRI," *J. Magn. Reson. Imag.*, 2014.
- [18] J. P. Kaipio, V. Kolehmainen, M. Vauhkonen, and E. Somersalo, "Inverse problems with structural prior information," *Inverse Problems*, vol. 15, pp. 713–730, 1999.
- [19] A. Borsic, W. R. B. Lionheart, and C. N. McLeod, "Generation of anisotropic-smoothness regularization filters for EIT," *IEEE Trans. Med. Imag.*, vol. 21, no. 6, pp. 579–587, Jun. 2002.
- [20] G. Barton, *Elements of Green's Functions and Propagation: Potentials, Diffusion, Waves*. Oxford, U.K.: Oxford Sci. Publications, 1989.
- [21] A. Tarantola, *Inverse Problem Theory: Methods for Data Fitting and Model Parameter Estimation*. New York: Elsevier, 1987.
- [22] M. Hanke and P. Hansen, "Regularization methods for large-scale problems," *Surv. Math. Ind.*, vol. 3, pp. 253–315, 1993.
- [23] P. C. Hansen, *Regularisation tools* 1992 [Online]. Available: <http://www.imm.dtu.dk/apch>, Dept. Math. Model., Tech. Univ. Denmark, Tech. Rep.
- [24] J. W. Thomas, *Numerical Partial Differential Equations: Finite Difference Methods*. New York: Springer, 1995, vol. 22.
- [25] A. Borsic and A. Adler, "A Primal-Dual Interior-Point framework for using the L1 or L2 norm on the data and regularization terms of inverse problems," *Inverse Problems*, vol. 28, no. 9, p. 095011, 2012.
- [26] A. Borsic, B. M. Graham, A. Adler, and W. R. Lionheart, "In vivo impedance imaging with total variation regularization," *IEEE Trans. Med. Imag.*, vol. 29, no. 1, pp. 44–54, Jan. 2010.
- [27] A. Savitzky and M. J. Golay, "Smoothing and differentiation of data by simplified least squares procedures," *Analyt. Chem.*, vol. 36, no. 8, pp. 1627–1639, 1964.
- [28] W. L. Briggs and S. F. McCormick *et al.*, *A Multigrid Tutorial*. Philadelphia, PA: SIAM, 2000.
- [29] E. E. Van Houten, M. I. Miga, J. B. Weaver, F. E. Kennedy, and K. D. Paulsen, "Three-dimensional subzone-based reconstruction algorithm for MR elastography," *Magn. Reson. Med.*, vol. 45, no. 5, pp. 827–837, 2001.